Analysis and simulations to obtain the weak magnetism term in ^{22}Na beta decay

Lutendo Phuthu

Department of Physics

University of the Western Cape

A thesis submitted in partial fulfillment for the degree of

Master of Science

2016

Declaration

I declare that ANALYSIS AND SIMULATIONS TO OBTAIN THE WEAK MAGNETISM TERM IN ^{22}Na BETA DECAY is my own work, that it has not been submitted for any degree or examination in any other university, and that all sources I have used or quoted have been indicated and acknowledged by complete references.

Lutendo Phuthu March 2016

Signature:

I dedicate this thesis to the one who is above, the Lord, who has been with me from the beginning of this journey to this point. He has been my strength and courage throughout the period of this work.

I would also like to dedicate this thesis work to my loving father, Thizwilondi Phuthu and my two sisters Marcia and Neani who have been very supportive to me throughout this journey. Lastly, I would like to dedicate this thesis to my late loving mother, I will forever be grateful to you.

Acknowledgements

My sincere gratitude to my supervisor, Smarajit Triambak who has been there for me throughout this work and whose door was always open for me at all times. The accomplishment of this work is the result of your commitment to helping me. I would like to thank Bernadette Rebeiro for all her help and for being a good advisor during the period of this work. I would also like to thank Bhivek Singh and Zandile Mabika who have been great office mates.

I am grateful to Angela Adams and Shirese Spannenberg of the Physics Department at the UWC for the administrative help they have provided when I needed them.

My sincere gratitude to my best friends Maano Denga, Mushe Maano and Tshililo Sidimela who have been very supportive and good cheerleaders. I would also like to thank the Kamp family, I will always appreciate what you have done for me.

Finally, I would like to thank the NRF for financial support during this time.

Abstract

The study of ^{22}Na beta decay offers an opportunity to test the Standard Model of Particle Physics via measurements of the $\beta-\gamma$ angular correlation. A previous measurement of this correlation yielded a non-zero value, indicating the need for a higher-order matrix element to the decay, beyond the allowed $V-A$ approximation. On assuming the Conserved Vector Current (CVC) hypothesis for weak interactions and using the magnetic dipole M1 width of the analog 2_1^+ state in ^{22}Na, one obtains an unexpectedly large 'second-class' form factor for ^{22}Na β decay that is in disagreement with the Standard Model prediction.

This thesis describes an analysis of data obtained from a previous ^{21}Ne(p,γ) experiment to obtain the M1 width of the 2_1^+ state of interest in ^{22}Na. This work aims to use the M1 width and the independently measured of the $\beta-\gamma$ angular correlation to obtain a higher-order Standard-Model-allowed weak magnetism form factor for the decay, in an attempt to explain the observed anomaly mentioned above.

Contents

List of Figures

Chapter 1

Introduction

The Standard Model of Particle Physics is a highly successful theory that describes elementary particles and their interactions at the most fundamental level. Yet, it leaves several questions unanswered. While there have been several proposed theoretical extensions to the current Standard Model, none of these have been experimentally verified to date. Thus, there is a lot of interest world-wide to look for experimental signatures of new physics, beyond the Standard Model. For example, the LHC experiment in CERN looks for these signatures by colliding very high energy protons with one another and observing the reaction products using large detectors such as ATLAS and CMS [1].

Complementary to the high-energy collider experiments mentioned above, one can make precise measurements of decay rates and correlations in atomic nuclei as probes for new physics. The challenging aspect in such experiments lies in understanding the structure of nuclei used for the measurements. This thesis describes one such work. In this work, we measure for the first time a $2^+ \rightarrow 3^+$ branch in the self-conjugate nucleus ^{22}Na. This transition, from the first 2^+ state to the ground state in ^{22}Na, has never been decisively observed before. The only reported measurement of the branch was performed using a $^{25}\mathrm{Mg}(p, \alpha\gamma)$ reaction, the results of which were never published, except in an internal laboratory report [2]. This result was used together with an independent $\beta - \gamma$ angular correlation experiment for ^{22}Na beta decay [3]

to obtain higher-order matrix elements for the decay, which were compared to Standard Model predictions. The analysis yielded an unexpectedly large 'induced-tensor' matrix element for the beta decay, which is forbidden in the Standard Model. In this work I describe a new measurement of the width of the $2_1^+ \rightarrow 3^+$ transition in ^{22}Na in an effort to explain this anomalous result.

Chapter 2

Weak Interactions and the Standard Model

It is apparent that Nature creates all its diversity with four known fundamental interactions that couple to twelve elementary particles. It has also been experimentally shown that the elementary particles are made of three generations of fermions called leptons and quarks (see Fig. 2.1), that interact with each other via the mediation of force carriers called the vector (spin-1) bosons. The gravitational force is purportedly mediated by a yet-to-be-discovered quantum of the gauge field called the graviton, electromagnetic interactions are mediated by photons, strong interactions by gluons and weak interactions by the Z^0 and $W^{\pm}$ bosons. The latest addition to these particles is the recently discovered Higgs particle which is a scalar (spin-0) boson and is responsible for giving the $W^{\pm}$ and Z^0 bosons their mass. This description, shown in Fig. 2.1 is part of a model called the Standard Model of Particle Physics, which in its present form excludes gravitational interactions [4].

In the study of nuclear physics, if one neglects gravity, the other three interactions are involved in a significant manner. The short-ranged strong interactions are responsible for binding the nucleons and quarks together in nuclei. The weak interactions govern β-decays and transforms the identity of the particle that decays, while the electromagnetic interactions play a crucial role in nuclear processes as nuclei have charge. Transitions between quantum states in nuclei lead to the emission of photons (γ-rays).

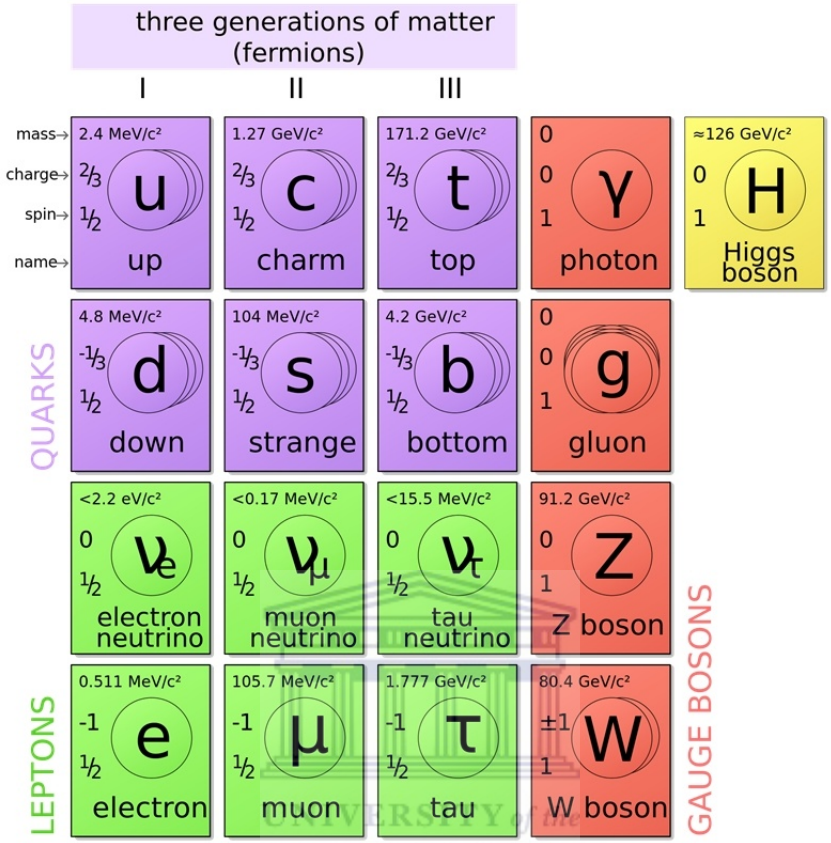

Figure 2.1: Elementary particles and their force carriers.

Radioactivity was first discovered by Becquerel in 1896, which marked the birth of nuclear physics. It became clear during that time that the decaying nuclei emitted three types of radiation, α (alpha), β (beta) and γ (gamma)-rays. In the 1920s it was understood that the β particles were electrons and the experimental data indicated that instead of being emitted with discrete energies, the electrons had a continuous energy spectrum (see Fig. 2.2). The continuous beta spectrum gave rise to two questions:

1. Why was the beta spectrum continuous?

2. Where do the electrons come from?

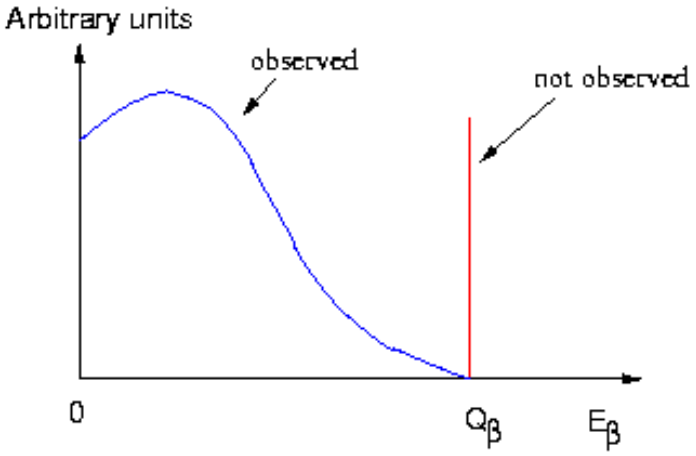

Figure 2.2: Energy distribution of electrons emitted in beta-decays.

The first question was answered by Pauli, who in trying to save fundamental conservation laws (such as energy, angular momentum, etc), suggested the existence of a new particle that is very light, neutral and had spin-1/2. He called it a 'neutron' [1]. Pauli assumed that this particle is emitted together with the electron and shared the energy released in the decay. In answering the second question, Fermi postulated that the electron and 'neutrino' [1] are created in the decay similarly as photons, which are emitted when nuclei undergo transitions from excited states to lower energy states [30].

There exist three different modes for β-decays in atomic nuclei.

$$n \rightarrow p + e^- + \tilde{\nu}_e \qquad (\beta^- \text{ decay})$$
$$p \rightarrow n + e^+ + \nu_e \qquad (\beta^+ \text{ decay})$$
$$p + e^- \rightarrow n + \nu_e \qquad (\text{electron capture decay})$$

where the particles ν_e and $\tilde{\nu}_e$ are the electron neutrino and anti-neutrino respectively. β^+ decays are energetically forbidden for free protons and can

[1]The neutron was not discovered till later, by Chadwick in 1932. The word 'neutrino' was coined by Enrico Fermi in 1934.

only occur for protons that are bound in nuclei.

The energy released in the β-decay process is given by its Q_β value,

$$\begin{aligned} Q_{\beta^-} &= [M(Z,A) - M(Z+1,A)]c^2 \\ Q_{\beta^+} &= [M(Z,A) - M(Z-1,A) - 2m_e]c^2 \\ Q_{EC} &= [M(Z,A) - M(Z-1,A)]c^2 - B \end{aligned} \tag{2.1}$$

where M represents atomic masses, A and Z are the mass number and atomic number respectively and B is the binding energy of the inner shell electrons.

2.1 Classification of nuclear β-decays

Since β-decay is governed by the weak interaction, perturbation theory can be used to describe the process. The transition rate W from an initial state to a final state for a given process is determined by the matrix element and the phase space according to the Fermi's golden rule [6]

$$W_{\alpha\to\beta} = \frac{2\pi}{\hbar}|M_{\beta\alpha}|^2 f(E) \ , \tag{2.2}$$

where $M_{\beta\alpha}$ is the matrix element that links the initial and final states and contains all the dynamical information, $f(E)$ is the phase space available for the decay and contains only the kinematical information. The latter can formally be obtained by performing the integral,

$$f(E) = \frac{V^2}{(2\pi\hbar)^6}\frac{d}{dE_{\max}}\int p_e^2 dp_e d\Omega_e p_{\tilde{\nu}}^2 dp_{\tilde{\nu}} d\Omega_{\tilde{\nu}} \ , \tag{2.3}$$

where V is the quantization volume and can be set equal to 1 (since the final results are independent of the volume). The maximum energy available for the decay is $E_{\max} \simeq Q_{EC}$ and is constant for specific decays. For massless neutrinos and a constant E_e, one obtains

$$E_{\tilde{\nu}} = p_{\tilde{\nu}} c \ , \tag{2.4}$$

$$\frac{dp_{\tilde{\nu}}}{dE_{\max}} = \frac{1}{c}\frac{dE_{\tilde{\nu}}}{dE_{\max}} = \frac{1}{c} \ , \tag{2.5}$$

so that the phase space in Eqn. (2.3) can be rewritten as

$$f(E) = \frac{d\Omega_e d\Omega_{\tilde{\nu}}}{(2\pi\hbar)^6 c} p_e^2 p_{\tilde{\nu}}^2 dp_e \ , \tag{2.6}$$

for a transition in which the electron has momentum between p_e and $p_e + dp_e$. We thus obtain from Eqns. (2.2) and (2.6),

$$W_{\alpha\to\beta} = \frac{1}{2\pi^3 c^3 \hbar^7} |M_{\beta\alpha}|^2 \int_{m_e c^2}^{E_{\max}} p_e^2 (E_{\max} - E_e)^2 dp_e \ . \tag{2.7}$$

Further integrating Eqn. (2.7) we obtain

$$W_{\alpha\to\beta} = \frac{1}{2\pi^3 c^3 \hbar^7} |M_{\beta\alpha}|^2 E_{\max}^5 \left[\frac{1}{30}\right] \ . \tag{2.8}$$

In describing the β decays, the normalized electron and neutrino wave functions have the form of plane waves

$$\psi_e = \frac{1}{\sqrt{V}} e^{\frac{i\vec{p}_e\cdot\vec{r}}{\hbar}} \qquad \psi_\nu = \frac{1}{\sqrt{V}} e^{\frac{i\vec{p}_\nu\cdot\vec{r}}{\hbar}}, \tag{2.9}$$

where

$$\begin{aligned} e^{\frac{i\vec{p}_e\cdot\vec{r}}{\hbar}} &= 1 + \frac{i\vec{p}_e\cdot\vec{r}}{\hbar} + \cdots \\ \text{and} \qquad e^{\frac{i\vec{p}_\nu\cdot\vec{r}}{\hbar}} &= 1 + \frac{i\vec{p}_\nu\cdot\vec{r}}{\hbar} + \cdots \ , \end{aligned} \tag{2.10}$$

with $\vec{p}_l$ being the momentum of the emitted lepton. Beta decays can be classified based on the orbital angular momentum transfered. Since both the electron and the neutrino have spin-1/2, they can couple to S = 0 or S = 1 states. If one assumes that the leptons are created at $\vec{r} = 0$ and that their wavefunctions do not vary appreciably over the nuclear volume, so that their de Broglie wavelength $\lambda >> R$ (nuclear size) and $|\vec{p}/\hbar| << 1$, then one can safely assume that the leptons carry no orbital angular momentum ($\ell = 0$) [7]. The higher order terms in Eqn. (2.10) can be neglected. This is called the allowed approximation. Within the allowed approximation, for

$\ell \geq 1$, the β-decay is forbidden to the first order. Thus, only the S-value contributes to the change in angular momentum of the nucleus in the decay. When $\Delta J = 0$, the β decay is called a Fermi decay and when $\Delta J = 1$ it is called a Gamow-Teller decay. When the momentum transfered is large in the decay, the allowed approximation breaks down and $\ell > 0$ terms can contribute. This is explained in more detail in Chapter 3.

2.2 Dirac equation and γ-matrices

The Schrödinger equation describes the dynamics of subatomic particles in non-relativistic quantum mechanics. However, in the case of β-decays since the neutrinos are nearly massless and the mass of the electron (positron) is much smaller than the energy released ($\sim$ MeV's), the theory of β-decay needs to be formulated relativistically. On accounting for spin, the wavefunctions involved are solutions to the Dirac equation, which has the following general form,

$$i\hbar\frac{\partial\psi}{\partial t} = \beta mc^2\psi - i\hbar c\boldsymbol{\alpha}\cdot\nabla\psi \ , \tag{2.11}$$

where β and $\boldsymbol{\alpha}$ are coefficients which are determined by physics conditions. Dirac obtained the following relations for $\boldsymbol{\alpha}$ and β

$$\begin{aligned} \alpha_i^2 &= \beta^2 = 1 \\ \{\alpha_i, \alpha_j\} &= 0 \\ \{\alpha_i, \beta\} &= 0 \ . \end{aligned} \tag{2.12}$$

The anticommutation relations showed that the coefficients α_i (i =1, 2, 3) and β cannot simply be just numbers. They are in fact matrices that operate on ψ, whose form is shown in Eqn. (2.20). Dirac showed that the smallest matrices that satisfy the requirement are of dimensionality 4×4. A particular choice used in describing these matrices is the Dirac-Pauli representation [4]

$$\alpha_i = \begin{pmatrix} 0 & \sigma_i \\ \sigma_i & 0 \end{pmatrix}, \qquad \beta = \begin{pmatrix} I & 0 \\ 0 & -I \end{pmatrix} \ , \tag{2.13}$$

where I is the unit 2×2 matrix and σ_i (i =1, 2, 3) are the Pauli matrices:

$$\sigma_1 = \begin{pmatrix} 0 & 1 \\ 1 & 0 \end{pmatrix}, \qquad \sigma_2 = \begin{pmatrix} 0 & -i \\ i & 0 \end{pmatrix}, \qquad \sigma_3 = \begin{pmatrix} 1 & 0 \\ 0 & -1 \end{pmatrix} \ . \tag{2.14}$$

Dirac introduced another way of dealing with these matrices by following notations [8]

$$\gamma^i = \beta\alpha_i \qquad and \qquad \gamma^0 = \beta \ . \tag{2.15}$$

These are the Dirac γ matrices, which can be written as a four-vector

$$\gamma^\mu = (\gamma^0, \gamma^i) \ . \tag{2.16}$$

The γ matrices satisfy the anticommutation relation

$$\{\gamma^\mu, \gamma^\nu\} = 2g^{\mu\nu} \ , \tag{2.17}$$

where μ and ν run from 0 to 3, and $g^{\mu\nu}$ is the metric tensor

$$g^{\mu\nu} = \begin{pmatrix} 1 & 0 & 0 & 0 \\ 0 & -1 & 0 & 0 \\ 0 & 0 & -1 & 0 \\ 0 & 0 & 0 & -1 \end{pmatrix} \ . \tag{2.18}$$

The Dirac equation described before can now be represented in a more compact form

$$i\hbar\gamma^\mu\partial_\mu\psi - mc\psi = 0 \ . \tag{2.19}$$

The ψ is now represented by a four component object called a Dirac spinor

$$\psi = \begin{pmatrix} \psi_1 \\ \psi_2 \\ \psi_3 \\ \psi_4 \end{pmatrix} \ , \tag{2.20}$$

where each component ψ_i $(i = 1, 2, 3, 4)$ satisfies the relativistic Klein-Gordon equation,

$$\left[\partial_\mu\partial^\mu + \left(\frac{mc}{\hbar}\right)^2\right]\psi_i = 0 \ , \tag{2.21}$$

with

$$E^2 = p^2c^2 + m^2c^4 \ . \tag{2.22}$$

2.3 Symmetries of the weak interaction

Fermi used the current-current structure of the electromagnetic interaction to explain the weak interaction, where the electromagnetic Hamiltonian is

$$H^{em} = -ej_\mu A_\mu \ , \tag{2.23}$$

where e (the electric charge) is the coupling constant, A_μ is the vector potential and j_μ is the electromagnetic current. By analogy, Fermi proposed that the Hamiltonian interaction for the beta decay has the form [30]

$$H^W = G \int d^3x (\bar{\psi}_p \hat{O} \psi_n)(\bar{\psi}_e \hat{O} \psi_\nu) \ , \tag{2.24}$$

where $\bar{\psi} = \psi^\dagger \gamma^0$, G is the weak coupling constant called the Fermi constant, that is determined by the experiment and $\hat{O}$ is the operator that characterizes the decay and is represented by bilinear covariant γ matrices. It turns out that one can build 16 linearly independent invariant 4×4 matrices by multiplying the γ-matrices, which have different transformation properties as shown in Table 2.1 below, where $\sigma^{\mu\nu} = \frac{i}{2}(\gamma^\mu\gamma^\nu - \gamma^\nu\gamma^\mu)$ and $\gamma^5 = i\gamma^0\gamma^1\gamma^2\gamma^3$.

Table 2.1: Possible combinations of bilinear covariant γ-matrices.

Transformation property	$\hat{O}_i$	No. of matrices
Scalar S	1	1
Vector V	γ^μ	4
Pseudo-Scalar P	γ^5	1
Axial-Vector A	$\gamma^\mu\gamma^5$	4
Tensor T	$\sigma^{\mu\nu}$	6

In 1956 one of the problems encountered in particle physics was the '$\tau - \theta$ puzzle'. The τ and θ particles appeared identical in every respect except in their decays. They decayed to states of opposite parities. This led Lee and Yang to propose that the weak interaction is not invariant under a parity transformation [9]. They also proposed experimental observables to look for parity violation in weak decays. The same year, Wu *et al.* performed a pioneering experiment to search for parity violation in the weak interaction [10]. They used the beta decay of polarized ^{60}Co (such that the nuclear

spins pointed in the same directions) nuclei and measured the distribution of the β particles relative to the parent polarization in the decay,

$$^{60}\mathrm{Co} \rightarrow ^{60}\mathrm{Ni} + e^{-} + \tilde{\nu} \ . \tag{2.25}$$

The surprising results from this experiment are shown in Fig. 2.3. Since parity conservation implies that the original and the results of parity transformation (mirror image) cannot be distinguished, the results of the experiment of Wu *et al*. showed that parity was maximally violated. As shown in Fig. 2.3 the spin remains unchanged under parity transformation but the momenta p_i of the electrons change sign. This gave direct evidence in favor of parity violation in the weak interaction.

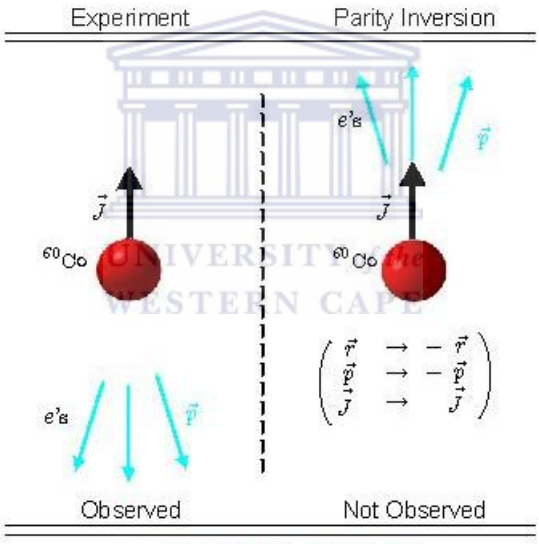

Figure 2.3: Sketch of the experimental results of Wu *et al* [10].

This experiment demonstrated one very useful symmetry in beta decays called helicity. Helicity is defined to be the projection of the spin $\vec{S}$ onto the direction of momentum, $\hat{p}$

$$h = \frac{\vec{S} \cdot \hat{p}}{|\vec{S}||\hat{p}|} \ . \tag{2.26}$$

Over time several experiments have shown that in beta decays only a single helicity is involved [11]. Electrons and neutrinos are always emitted left-handed (with helicity -1), while positrons and antineutrinos are emitted right-handed (with helicity +1). Based on this experimental evidence, if one considers a weak interaction that only couples to left-handed particles, one can project out negative helicity states with the projection operators

$$\hat{P}_{-} = \frac{1}{2}(1 - \gamma^5) \ . \tag{2.27}$$

There is another symmetry similar to parity that is called charge conjugation. The charge conjugation operation changes the charge of a particle and leaves the spin and momentum unchanged. It has the property of converting a particle to its antiparticle, such that

$$C|q\rangle = |-q\rangle \ . \tag{2.28}$$

Like parity, charge conjugation is also violated in the weak interaction. When C is applied to a neutrino (which is left-handed) it gives a left-handed antineutrino, which has not been experimentaly found so far. Thus, antineutrinos have the opposite helicity and are right-handed.

In the present scheme of the Standard Model, the experimental evidence points that the weak interaction excludes all couplings shown in Table. 2.1 except the vector V and the axial-vector A. This is called the $V - A$ law of weak interactions. The interaction Hamiltonian described in Eqn. (2.24) can now be written as,

$$H^W = \frac{G}{\sqrt{2}} \int d^3x \underbrace{\left[\bar{\psi}_p \gamma^\mu (c_V + c_A \gamma^5) \psi_n\right]}_{\text{hadronic current}} \underbrace{\left[\bar{\psi}_e \gamma^\mu (1 - \gamma^5) \psi_\nu\right]}_{\text{leptonic current}} + h.c. \ , \tag{2.29}$$

where c_V and c_A are called the vector and axial vector coupling constants respectively.

Chapter 3

Electromagnetic transitions in nuclei

Electromagnetic transitions in nuclei manifest themselves via the emission of γ-radiation and are an essential tool for studying the structure of nuclei and for testing nuclear models. Below I describe one such very successful model called the nuclear shell model, before discussing electromagnetic properties in nuclei.

3.1 Nuclear Shell Model

The nuclear shell model was adopted in analogy to the atomic shell model in order to describe nuclei. The idea of a shell model involves the filling of orbits with nucleons in a shell structure with increasing energy within a potential. The discovery of enhanced binding energies at specific magic numbers (2, 8, 28, 50, 82, 126, ...) provided ample evidence for the nuclear shell structure. Nuclei with a magic number of neutrons and protons (or both) exhibited properties of closed shells, analogous to inert gas atoms that have completely filled electronic shells. The binding energy of nuclei with magic numbers were experimentally determined to be much greater than the neighbouring nuclei. It is also experimentally known that the first excited states in magic nuclei are comparatively much higher in energy [12].

The shell model assumes that nucleons move freely in orbits in nuclei while

experiencing an average central potential. In the independent particle shell model, the nuclear Hamiltonian is given by [13],

$$\hat{H} = \hat{H}_0 + \hat{V} \ , \tag{3.1}$$

where $\hat{V}$ is a residual interaction and $\hat{H}_0$ is the summed single-particle Hamiltonian,

$$\hat{H}_0 = \sum_{i=1}^{A} \hat{h}_i \ , \tag{3.2}$$

where $\hat{h}_i$ governs the motion of the i'th nucleon and $\hat{H}_0$ corresponds to a system of individual particles moving independently in a potential. A simple single-particle Hamiltonian can be defined as

$$\hat{h}_i = \frac{\hat{p}_i^2}{2M} + U(r_i) \ , \tag{3.3}$$

where $\hat{p}_i$ (=-$i\hbar\vec{\nabla}$) is the momentum of the nucleon, M is the mass of the nucleon, $U(r)$ is the central single-particle potential.

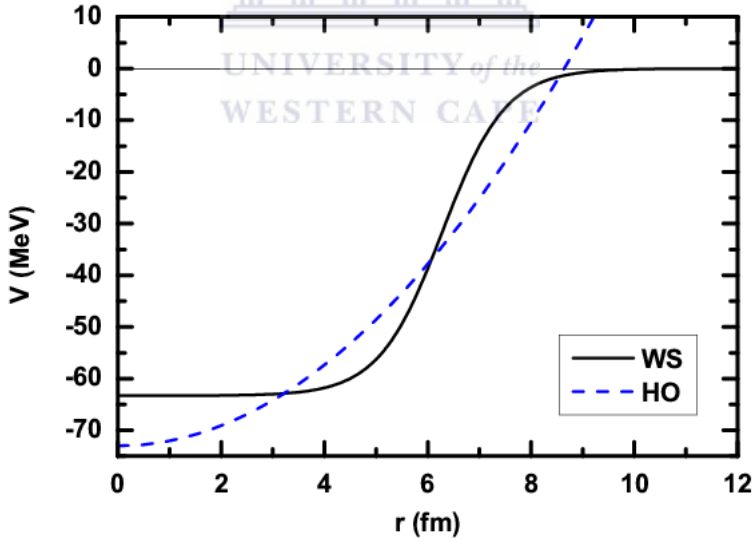

Figure 3.1: Single-particle shell model potentials: Harmonic oscillator and Woods-Saxon.

In order to obtain solutions to the non-relativistic Schrödinger equation for the Hamiltonian $\hat{H}$, it is natural to start with potentials whose solutions can

be obtained analytically. Justifiably good starting points to obtain the single particle wavefunctions are the simple harmonic oscillator and infinite square well potentials. However the infinite square-well is not a good approximation for the nuclear potential because it has sharp edges and it requires an infinite amount of energy to take a nucleon out of the well. The harmonic oscillator on the other hand does not have a sharp edge, yet it still requires infinite separation energies [14].

Apart from these two potentials, there is the Woods-Saxon potential that appears to be more realistic and is given as,

$$U(r) = \frac{-V_0}{1 + exp(r - R/a)} \ , \tag{3.4}$$

where the mean radius $R = 1.25A^{1/3}$ fm, the half distance $a = 0.524$ fm, V_0 is of order 50 MeV. The comparison of solutions obtained from the harmonic oscillator and Wood-Saxon potentials is shown on the left side of Fig. 3.2. The harmonic oscillator potential has obvious problems as it monotonically increases with r, unlike how a short-ranged nuclear force should behave. Though the Wood-Saxon potential seems to be a reasonable potential, it turns out that it can only reproduce the magic numbers 2, 8 and 20. As shown in Fig. 3.2, the Wood-Saxon potential suggests that the next magic number be 40 instead of the experimental known value of 50. The solution to this discrepancy lies in the spin-orbit coupling [15]. The spin-orbit potential has the form,

$$V_{so}(r)\vec{\ell} \cdot \vec{s} \ , \tag{3.5}$$

where $\vec{\ell}$ is the orbital angular momentum and $\vec{s}$ is the intrinsic spin of the nucleon. The $\vec{\ell} \cdot \vec{s}$ factor causes the reordering of the single-particle levels. The expectation value of $\vec{\ell}.\vec{s}$ can be obtained from the following expression [14],

$$\begin{aligned} j^2 &= (\vec{\ell} + \vec{s})^2 \\ j^2 &= \ell^2 + 2\vec{\ell} \cdot \vec{s} + s^2 \\ \vec{\ell} \cdot \vec{s} &= \frac{1}{2}(j^2 - \ell^2 - s^2) \ . \end{aligned} \tag{3.6}$$

Hence

$$\langle \vec{\ell} \cdot \vec{s} \rangle = \frac{1}{2}[j(j+1) - l(l+1) - s(s+1)]\hbar^2 \ . \tag{3.7}$$

The single-particle energies obtained after the spin-orbit potential was added to the Wood-Saxon potential are shown on the right-hand side of Fig. 3.2. Clearly, the addition of the spin-orbit potential reproduces the experimental magic numbers up to 126 satisfactorily. This is an example of the single-particle shell model. In the extreme single particle shell model it is assumed that only the valence (unpaired) nucleon contributes to the properties of a nucleus. The nucleons occupying filled shells form part of an 'inert core'.

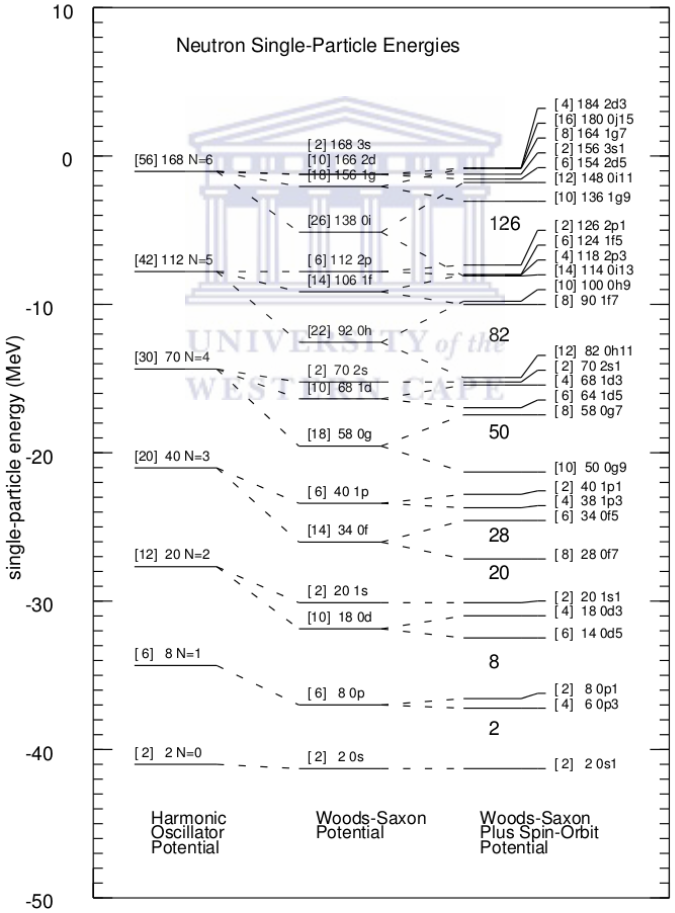

Figure 3.2: Single-particle shell model for the harmonic oscillator, Woods-Saxon with and without spin-orbit potentials.

3.2 Electromagnetic moments

Consider a system with a continuous charge distribution $\rho(\vec{r}\,')$. The electrostatic potential due to this distribution is then given by Coulomb's law [16],

$$V = \int \frac{\rho(\vec{r}\,')}{|\vec{r} - \vec{r}\,'|} d\vec{r}\,' \ , \tag{3.8}$$

with

$$\frac{1}{|\vec{r} - \vec{r}\,'|} = \left[(x - x')^2 + (y - y')^2 + (z - z')^2\right]^{-1/2} \ . \tag{3.9}$$

Eqn. (3.9) can be expanded in a Taylor series for 3 variables,

$$f(t, u, v) = \sum_{n=0}^{\infty} \frac{1}{n!} \left[t\frac{\partial}{\partial t} + u\frac{\partial}{\partial u} + v\frac{\partial}{\partial v} \right]^n \ , \tag{3.10}$$

with the derivatives calculated at $t = 0$, $u = 0$, $v = 0$. Using Eqn. (3.10) for the source coordinates ($t = x'$, etc), Eqn. (3.8) becomes

$$V = \frac{\int \rho(\vec{r}\,')d\vec{r}\,'}{r} + \frac{x_i \int x_i' \rho(\vec{r}\,')d\vec{r}\,'}{r^3} + \frac{1}{2}\frac{x_i x_j \int (3x_i' x_j' - r'^2\delta_{ij})\rho(\vec{r}\,')d\vec{r}\,'}{r^5} + \cdots \ , \tag{3.11}$$

where $(x_1, x_2, x_3) \equiv (x, y, z)$. One can define the terms in Eqn. (3.11) as follows

$$q = \int \rho(\vec{r}\,')d\vec{r}\,' \ , \tag{3.12}$$

$$\vec{p} = \int \vec{r}\,' \rho(\vec{r}\,')d\vec{r}\,' \ , \tag{3.13}$$

$$Q_{ij} = \int (3x_i' x_j' - r'^2\delta_{ij})\rho(\vec{r}\,')d\vec{r}\,') \ . \tag{3.14}$$

The first term q is called the monopole term and is identical to the potential of a charge placed at the origin. The second term p has the potential of a dipole and is called the electric dipole moment vector and Q_{ij} are the components of the electric quadrupole moment tensor. Such an expansion of multipoles continues with the increase of powers in the denominator (octupole, hexadecapole, etc). We can then rewrite Eqn. (3.11) as,

$$V = \frac{q}{r} + \frac{\vec{p} \cdot \vec{\mathrm{x}}}{r^3} + \frac{1}{2}\frac{Q_{ij} x_i x_j}{r^5} + \cdots \ . \tag{3.15}$$

The above multipole expansion can be used for the Coulomb potential created by protons in nuclei. To do so we must now consider a quantum system where the charge density $\rho(\vec{r}\,')$ is understood as Ze times the probability density of finding a proton at point $\vec{r}\,'$. For atomic nuclei, parity conservation demands that the electric dipole term in Eqn. (3.13) vanishes [17], which leaves the leading-order charge distribution in the nucleus to arise from the quadrupole term Q_{ij}.

$$Q_{ij} = \int (3x'_i x'_j - r'^2 \delta_{ij}) Ze\psi^*(\vec{r}\,')\psi(\vec{r}\,')d\vec{r}\,' \ . \tag{3.16}$$

In a similar manner, a localized current distribution $\vec{J}(\vec{r}\,')$ gives a vector field with a vector potential $\vec{A}$, which can be expressed as a multipole expansion as well. The monopole term for this case vanishes and so do the other even powers of r using similar parity conservation arguments as before. The lowest order term in the expansion is [16]

$$\vec{A} = \frac{\vec{\mu} \times \vec{r}}{r^3} + \cdots \ , \tag{3.17}$$

where $\vec{\mu}$ is the magnetic dipole moment given by

$$\vec{\mu} = \frac{1}{2} \int \vec{r} \times \vec{J}(\vec{r}\,')d^3\vec{r}\,'. \tag{3.18}$$

We discuss these two special cases in the sections below.

3.2.1 Electric quadrupole

From Eqn. (3.16), one can drop the charge Ze of the nucleus to give the quadrupole moment term the dimension of area (which is usually in barns). If the charge distribution has an axial symmetry with respect to the $\hat{z}$-axis, the components of Eqn. (3.16) can be reduced to one. The quadrupole moment can be written as

$$Q = \int (3z'^2 - r'^2)\psi^*(\vec{r}\,')\psi(\vec{r}\,')d\vec{r}\,' \ . \tag{3.19}$$

As an example, for an odd Z, even N nucleus, the valence proton wavefunction, for $l = m$ is,

$$\psi = \frac{U_l(r)}{r} Y_l^l(\theta, \phi) \ . \tag{3.20}$$

Therefore, the maximum observable quadrupole moment is

$$Q = \int U_l^2(r)|Y_l^l(\theta,\phi)|^2 r^2(3\cos^2\theta - 1)\sin\theta dr d\theta d\phi \tag{3.21}$$

or

$$Q = \langle r^2\rangle \int |Y_l^l(\theta,\phi)|^2(3\cos^2\theta - 1)\sin\theta d\theta d\phi \ , \tag{3.22}$$

with

$$Y_l^l(\theta,\phi) = (-1)^l\sqrt{\frac{2l+1}{4\pi}}\frac{1}{(2l)!}e^{il\phi}(\sin\theta)^l\frac{(2l)!}{2^l l!} \ . \tag{3.23}$$

In general, for any given j, the quadrupole moment in nuclei due to a single proton can be written as,

$$Q = -\langle r^2\rangle\frac{2j-1}{2j+2} \ . \tag{3.24}$$

One can assume that the valence nucleon lies on the surface, therefore $\langle r^2\rangle$ is the mean square distance of a nucleon from the center of the nucleus,

$$\langle r^2\rangle = R^2 = r_0^2 A^{2/3} \ . \tag{3.25}$$

It should be noted that Eqn. (3.24) is for both $j = l + 1/2$ and $j = l - 1/2$. It can also be seen that for $j = 1/2$, the quadrupole moment Q is zero. Evidence shows that the electric quadrupole moments of even-even nuclei with $j = 0$ are identically zero [16]. These statements can be generalized by saying that $Q = 0$ unless $j \geq 1$.

3.2.2 Magnetic dipole

In a nucleus, magnetic moments are formed by the orbital motion of the protons and the intrinsic spin of the nucleons that induces their own magnetic moments. Thus, the magnetic dipole moment is then given by the expectation value of

$$\mu_z = [l_z g^l + s_z g^s]\mu_N \ , \tag{3.26}$$

where μ_N is the nuclear magneton given by

$$\mu_N = \frac{e\hbar}{2m_p} \ , \tag{3.27}$$

with m_p the mass of the proton. The gyromagnetic (g) factors for nucleons are given by

$$\begin{aligned} g_p^l &= 1 \qquad g_p^s = 5.58 \\ g_n^l &= 0 \qquad g_n^s = -3.82 \ . \end{aligned} \tag{3.28}$$

As mentioned before, in the extreme single-particle shell model, the properties of odd-A nuclei near closed shells are simply described by the characteristics of the unpaired valence nucleon. One can evaluate the magnetic moment of such a nucleus as [17],

$$\mu(j = l \pm 1/2) = \Big[j \Big(g_l \pm (g_s - g_l) \frac{1}{2l+1} \Big) \Big] \mu_N \ . \tag{3.29}$$

Equations (3.29) are called the Schmidt values and the lines that gives μ as a function of the angular momentum are called the Schmidt lines. It can also be seen from equation (3.29) that for each nucleon there will be two Schmidt lines, corresponding to $j = l + 1/2$ and $j = l - 1/2$, respectively [16]. These are shown in Fig. 3.3.

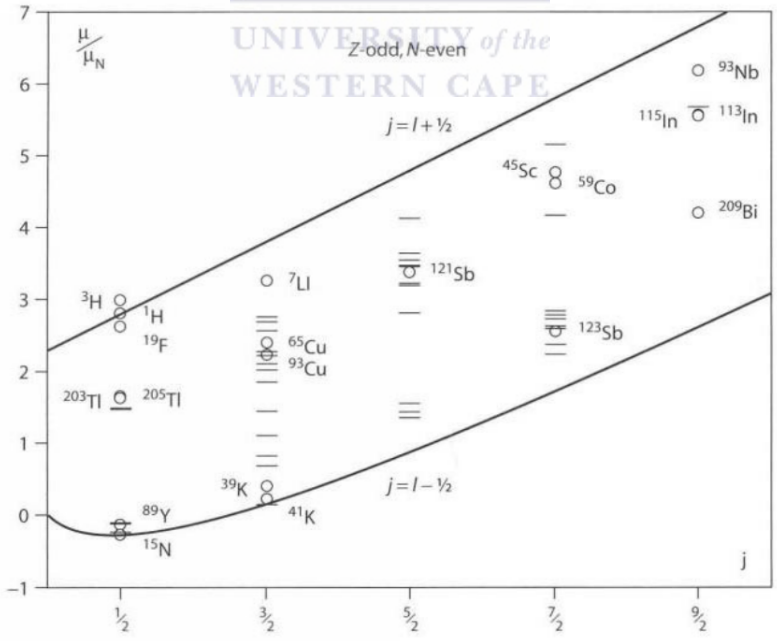

Figure 3.3: The magnetic moments μ as a function of the angular momentum for odd proton nuclei.

3.3 Electromagnetic transition probabilities in nuclei

Just like in β-decays, the electromagnetic transition rate W of an initial state to a final state for a given process is determined by the matrix element and the phase space available $f(E)$ using Fermi's golden rule,

$$W = \frac{2\pi}{\hbar}|\langle\phi_k(\vec{r})|H'|\phi_0(\vec{r})\rangle|^2 f(E) \ , \tag{3.30}$$

where $\phi_0(\vec{r})$ and $\phi_k(\vec{r})$ are the initial and final wave functions respectively. The transition probability is related to the width of a state Γ by the following

$$W = 1/\tau \tag{3.31}$$

$$\Gamma\tau = \hbar \ , \tag{3.32}$$

where τ is the mean lifetime of the state. In Eqn. (3.30) H' is the perturbing electromagnetic Hamiltonian,

$$H' = -j_\mu A_\mu \ , \tag{3.33}$$

where $A_\mu = (\phi, \vec{A})$ is the 4-vector potential and $J_\mu = (\rho, \vec{j}/c)$ is the current density. Since H' in Eqn. (3.33) is a scalar, only multipoles of the same order in both $\vec{j}$ and $\vec{A}$ can be coupled together to form an angular momentum zero operator. For this purpose, one can write the radiation field in terms of eigenfunctions of angular momentum operators [17],

$$\vec{A}(\vec{r}, t) = \sum_{\lambda\mu} \vec{A}_{\lambda\mu}(\vec{r}, t) \ , \tag{3.34}$$

where the vector functions of spherical tensor ranks (λ, μ) satisfy the relation

$$\vec{J}^{\,2}\vec{A}_{\lambda\mu}(\vec{r}, t) = \lambda(\lambda+1)\vec{A}_{\lambda\mu}(\vec{r}, t) \qquad \vec{J}_0\vec{A}_{\lambda\mu}(\vec{r}, t) = \mu\vec{A}_{\lambda\mu}(\vec{r}, t) \ . \tag{3.35}$$

$\vec{A}_{\lambda\mu}(\vec{r}, t)$ can be expressed in terms of the spherical harmonics $Y_{\lambda\mu}(\theta, \phi)$ allowing two different types of multipoles called the electric multipole $(E\lambda)$

and magnetic multipole ($M\lambda$), and relate to the spherical harmonics in the following manner

$$A_{\lambda\mu}(E\lambda,\vec{r}) = -\frac{i}{k}\nabla\times(\vec{r}\times\nabla)(j_\lambda(kr)Y_{\lambda\mu}(\theta,\phi))$$
$$A_{\lambda\mu}(M\lambda,\vec{r}) = (\vec{r}\times\nabla)(j_\lambda(kr)Y_{\lambda\mu}(\theta,\phi)) \ , \tag{3.36}$$

where $j_\lambda(kr)$ is a spherical Bessel function. When γ-rays are emitted in electromagnetic transitions, they carry an orbital angular momentum λ. Since photons are massless and carry a helicity of ±1 and spin 1, they can only have two polarization states for a given momentum $\hbar k$. The angular momentum for a transition between initial and final states J_i and J_f has to be conserved, so that

$$\vec{J_i} = \vec{\lambda} + \vec{J_f} \ . \tag{3.37}$$

Parity is also conserved similarly

$$\pi_i = \pi_\gamma\pi_f \ . \tag{3.38}$$

The conservation of the angular momentum leads to the selection rule

$$|J_i - J_f| \leq \lambda \leq J_i + J_f \ . \tag{3.39}$$

This relation gives all the possible values of λ. A γ-ray transition of rank $\lambda = 1$ is called a dipole, $\lambda = 2$ is called a quadrupole and so on [17].

The parity of the γ-ray in nuclear transition with the electric nature is given by

$$\pi(E\lambda) = (-1)^\lambda \ , \tag{3.40}$$

while for magnetic transitions, the parity is given by

$$\pi(M\lambda) = (-1)^{\lambda+1} \ . \tag{3.41}$$

Using Eqn. (3.36), the multipole parts (λ,μ) of H' can be written as

$$O_{\lambda\mu}(E\lambda) = -\frac{i(2\lambda+1)!!}{ck^{\lambda+1}(\lambda+1)}\vec{j}(\vec{r})\cdot\nabla\times(\vec{r}\times\nabla)(j_\lambda(kr)Y_{\lambda\mu}(\theta,\phi))$$
$$O_{\lambda\mu}(M\lambda) = -\frac{(2\lambda+1)!!}{ck^{\lambda}(\lambda+1)}\vec{j}(\vec{r})\cdot(\vec{r}\times\nabla)(j_\lambda(kr)Y_{\lambda\mu}(\theta,\phi)) \ . \tag{3.42}$$

The transition probability for multipole λ from an initial state to final state now takes the form,

$$W(\lambda, J_i \to J_f) = \frac{8\pi(\lambda+1)}{\lambda[(2\lambda+1)!!]^2}\frac{k^{2\lambda+1}}{\hbar}B(\lambda, J_i \to J_f) \ , \tag{3.43}$$

where the reduced transition probability $B(\lambda, J_i \to J_f)$ is written in terms of multipole operator,

$$B(\lambda, J_i \to J_f) = \frac{1}{2J_i+1}|\langle J_f||O_\lambda||J_i\rangle|^2 \ . \tag{3.44}$$

One can make simple estimates of electromagnetic transition rates by assuming that the transition occurs from one state to another by a single nucleon moving from one single-particle orbit to another in a central potential. These are called the single-particle Wiesskopf estimates of transition probability. These estimates yield the transition strengths

$$\begin{aligned} B_W(E\lambda) &= \frac{1}{4\pi}\left(\frac{3}{\lambda+3}\right)^2 (1.2)^{2\lambda}A^{2\lambda/3}e^2 fm^{2\lambda} \\ B_W(M\lambda) &= \frac{10}{\pi}\left(\frac{3}{\lambda+3}\right)^2 (1.2)^{2\lambda-2}A^{(2\lambda-2)/3}\mu_N^2 fm^{2\lambda-2} \ , \end{aligned} \tag{3.45}$$

for electric and magnetic transitions of a given order λ.

3.4 Isospin selection rules in electromagnetic transitions.

In 1932, after the discovery of the neutron, Werner Heisenberg introduced the concept of isospin symmetry. In a manner similar to electron spin, he proposed the proton and the neutron to be different projections of a 'nucleon', such that

$$|p\rangle = \begin{pmatrix} 1 \\ 0 \end{pmatrix} \qquad \text{and} \qquad |n\rangle = \begin{pmatrix} 0 \\ 1 \end{pmatrix} \ , \tag{3.46}$$

where $|p\rangle$ and $|n\rangle$ correspond to different isospin states of the nucleon. This assumption should not be surprising as both of them are spin-$\frac{1}{2}$ Fermions with a mass difference of $\approx 0.1\%$ between them. This concept of isospin

tells us that they (protons and neutrons) can be considered as identical particles in the absence of the electromagnetic interaction. They can only be distinguished by their electromagnetic properties. Thus the nuclear force is assumed to be charge independent, i.e. it is the same irrespective of whether a nucleon is a proton or neutron. Since the nucleons cannot be distinguished from each other purely based on the strong interaction, this symmetry is called isospin symmetry.

One can define the Pauli isospin matrices for the algebra of isospin [18]

$$\vec{t} = \frac{1}{2}\vec{\tau} \qquad \text{and} \qquad t_z = \frac{1}{2}\tau_z \ , \tag{3.47}$$

where

$$\tau_x = \begin{pmatrix} 0 & 1 \\ 1 & 0 \end{pmatrix}, \qquad \tau_y = \begin{pmatrix} 0 & -i \\ i & 0 \end{pmatrix}, \qquad \tau_z = \begin{pmatrix} 1 & 0 \\ 0 & -1 \end{pmatrix} \ , \tag{3.48}$$

such that the following can be obtained

$$\begin{aligned} t_z|p\rangle &= \frac{1}{2}\tau_z|p\rangle \\ &= \frac{1}{2}|p\rangle \qquad \Rightarrow t_z = \frac{1}{2} \end{aligned} \qquad \text{(for proton)}$$

$$\begin{aligned} t_z|n\rangle &= \frac{1}{2}\tau_z|n\rangle \\ &= -\frac{1}{2}|n\rangle \qquad \Rightarrow t_z = -\frac{1}{2} \ . \end{aligned} \qquad \text{(for neutron)}$$

Since both the proton and neutron are isospin $t = \frac{1}{2}$ particles and from the above expressions it is clear that the they can be distinguished by the third component of the isospin operator t_z (which relates to the nucleon charge).

The isospin of a nucleus is given by the total isospin [19]

$$T = \sum_{k=1}^{A} t_k \qquad \text{and} \qquad T_z = \sum_{k=1}^{A} t_z = \frac{1}{2}(Z - N) \ , \tag{3.49}$$

where the value of T_z ranges from $-T \leq T_z \leq T$, similar to angular momentum.

The isospin plays an important role in the electromagnetic transitions. Consider an electric dipole transition. The electric dipole operator is given by

$$\begin{aligned}\hat{O}(E1) &= e\sum_{i=1}^{Z}\hat{z}_i \\ &= e\frac{1}{2}\sum_{k=1}^{A}(\tau_{z_k}+1)z_k \\ &= \frac{1}{2}e\sum_{k=1}^{A}\tau_{z_k}z_k + e\frac{1}{2}\sum_{k=1}^{A}z_k \ . \end{aligned} \tag{3.50}$$

The first term in the above is an isovector and the second term is an isoscalar. The isoscalar term depends on the position of the centre of mass of the whole nucleus and does not cause transitions in nuclei. The isovector term leads to the selection rule,

$$|T_i - T_f| \leq 1 \leq T_i + T_f \ . \tag{3.51}$$

This implies that $\Delta T = 1$ electromagnetic transitions are allowed, while $\Delta T = 0$ transitions are forbidden assuming isospin is a good quantum number [18].

Now consider a magnetic dipole. The magnetic moment $\vec{\mu}$, in units of the nuclear magneton for a nucleus can be written using isospin formalism [18],

$$\hat{O}(M1) = \vec{\mu} = \sum_{k=1}^{A}\frac{1}{2}(\tau_{z_k}+1)(g_p\vec{s}_k + \vec{l}_k) + \frac{1}{2}(\tau_{z_k}+1)g_n\vec{s}_k \tag{3.52}$$

which, for the values in Eqn. (3.28) reduces to

$$\hat{O}(M1) = \vec{\mu} = \frac{1}{2}\vec{J} + 0.38\sum_{k=1}^{A}\vec{s}_k + \sum_{k=1}^{A}\tau_z(k)(4.71\vec{s}_k + \frac{1}{2}\vec{J}_k) \ . \tag{3.53}$$

The first term clearly does not contribute to transitions between states. The second term is isoscalar and the last term is isovector. It is obvious from Eqn.(3.53) that the isoscalar term is much weaker in comparison to the isovector term. This leads to the isospin selection rule that $\Delta T = 1$ $M1$ transitions are much stronger than $\Delta T = 0$ M1 transitions.

3.5 Multipole mixing

If only one multipole contributes to a transition, then a measurement of its lifetime allows the extraction of the transition matrix element. However, it is entirely possible, that, even though in general magnetic transition probabilities are much smaller than electric transition probabilities, one could have transitions where the $E(\lambda+1)$ and $M\lambda$ strengths are comparable. In such a situation one can only extract useful nuclear structure information by making an additional measurement of the multipole mixing ratio in the transition by measurements of the angular distribution or angular correlation of the photons. The mixing ratio is defined as

$$\delta^2 = \frac{W(E(\lambda+1))}{W(M\lambda)} \ . \tag{3.54}$$

The angular distribution of an emitted γ-ray depends on the initial magnetic substate m_i and the final magnetic substate m_f. Consider a dipole transition from initial state of $J_i = 1$ to a final state of $J_f = 0$ as an example. The magnetic substates can take values m_i = -1, 0, 1 and $m_f = 0$. In the case of $m_i = 0 \rightarrow m_f = 0$, the gamma emission probability varies as $\sin^2\theta$ (where θ is the angle defined with respect to the quantization axis). For $m_i = \pm 1 \rightarrow m_f = 0$ transitions, the angular distribution of the gammas goes as $\frac{1}{2}(1+\cos^2\theta)$. Thus an anisotropy in the gamma-ray angular distribution can easily be introduced by creating unequal populations of the magnetic substates.

In general, a multipole mixing ratio can be obtained from the angular distribution of γ-rays. A measured angular distribution for point detectors, with different multipoles is [20]

$$W(\theta) = \sum_{K=\text{even}} a_K P_K(\cos\,\theta) \ , \tag{3.55}$$

where the a_K's contain the multipolarity information of the observed γ-ray and $P_K(\cos\theta)$ are the Legendre polynomials. Eqn. (3.55) can be averaged

over the face of a finite size detector, so that the response of a detector is

$$R = \frac{\sum a_K \int P_K(\cos\,\theta)\varepsilon d\Omega}{\int \varepsilon d\Omega} \ , \tag{3.56}$$

where ε is the detection efficiency of the incident gamma-ray. This equation can be rewritten for cylindrically symmetric detectors with the introduction of attenuation coefficients, so that the distribution is

$$R = \sum_{K=\text{even}} a_K Q_K P_K(\cos\,\theta) \ , \tag{3.57}$$

where Q_K are the attenuation coefficients due to the detector solid angle.

Chapter 4

Relation between the weak and the electromagnetic interactions

Within the Standard Model of Particle Physics both electromagnetism and the weak interactions are described in a unified manner as different components of the 'electroweak' force [21]. In this chapter I describe some aspects of electroweak symmetry, with experimental examples to motivate the work done in this thesis.

4.1 Conservation of the weak vector current

It is well established that the electric charge is a conserved quantity, even in the presence of strongly interacting forces (such as gluon exchanges between quarks). Another way of stating this conservation law is that the coupling constant in Eqn. (2.23) is not renormalized in a strongly interacting medium. For example, within the quark model, the electromagnetic current density is given by [21]

$$j_\mu^{EM} = \frac{2}{3}\bar{\psi}_u\gamma_\mu\psi_u - \frac{1}{3}\bar{\psi}_d\gamma_\mu\psi_d + \dots \ . \tag{4.1}$$

Analogously, the weak interaction current is given by

$$j_\mu^W = V_\mu + A_\mu = \bar{\psi}\gamma_\mu(1-\gamma^5)\psi \ , \tag{4.2}$$

with the vector part of the interaction $V_\mu = \bar{\psi}\gamma_\mu\psi$ and the axial vector part $A_\mu = \bar{\psi}\gamma_\mu\gamma^5\psi$. If we make a substitution for electric charge in terms of the Pauli isospin matrices and separate the isoscalar and isovector components like we did in Section 3.4, then the isovector part of the electromagnetic current can be written as $j_\mu^{EM} = \frac{1}{2}\left(\bar{\psi}\gamma_\mu\tau_z\psi\right)$, up to a constant multiplicative factor. Analogously, as the charge changes by one unit in a β decay, the vector part of the weak interaction can be described as $V_\mu = \left(\bar{\psi}\gamma_\mu\tau^{\pm}\psi\right)$, where the ψ's represent quark or nucleon states in Dirac notation. This similarity between the isovector electromagnetic current and the weak vector current, together with available experimental data, led Feynman and Gell-mann to postulate the Conserved Vector Current (CVC) hypothesis [22]. Two direct outcomes of the CVC hypothesis are the following:

1. The vector coupling constant is not renormalized in a strongly interacting medium and is a conserved quantity, similar to the electric charge as mentioned previously.

2. Analogous β and γ transitions in nuclei have matrix elements that are proportional to one another [23]

The CVC hypothesis is an integral part of the Standard 'electroweak' Model. In the description of the nuclear β decays, the CVC hypothesis plays an important role in the studies of pure Fermi decays and in searches for interactions that are not included in the minimal Standard Model. One such example arises in the hadronic part of the current-current interaction for nucleon/nuclear β decay. This is described below.

4.2 Form factors in semi-leptonic decays

Unlike the leptons, nucleons are not point particles. Instead they have an internal structure. They are composed of three quarks which can either be u,u,d (proton) or u,d,d (neutron). As shown in Fig. 4.1, the quarks interact with each other via the exchange of gluons in the strong interaction. The interference of the strong interaction in the β-decay induces additional

terms in the vector and axial-vector current structure of the hadronic part of Eqn. (2.29). Consider a simple decay such as a $J^\pi = 1/2^+ \rightarrow J^\pi = 1/2^+$ neutron decay.

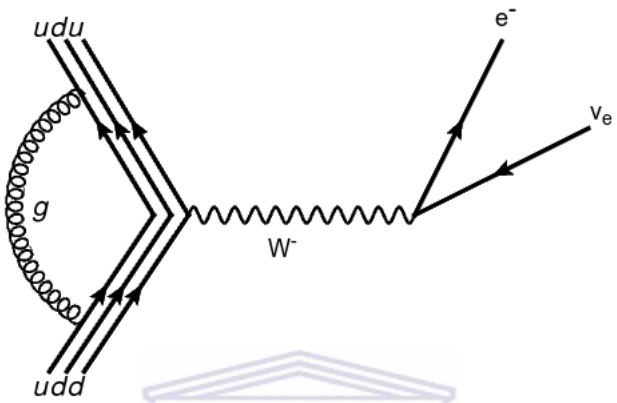

Figure 4.1: A nuclear beta decay is essentially the transformation of one quark to another via the weak interaction. The decay occurs in a sea of gluons that strongly interact with the quarks.

The matrix element of the hadronic weak current, which should be Lorentz invariant, is allowed to have the induced terms [21],

$$\begin{aligned}\langle\beta|h_\mu^W|\alpha\rangle &= \bar{\psi}(p_2)\Big[\gamma_\mu(g_V + g_A\gamma_5) - \frac{i}{2M}\sigma_{\mu\nu}q^\nu(g_M + g_T\gamma_5) \\ &\quad + \frac{q_\mu}{2M}(g_S - g_P\gamma_5)\Big]\psi(p_1)\ , \end{aligned} \tag{4.3}$$

where $\bar{\psi}(p_2)$ and $\psi(p_1)$ are Dirac spinors and q is the four-momentum transfered

$$q = p_1 - p_2\ . \tag{4.4}$$

In the above,

$$M = \frac{1}{2}(M_1 + M_2)\ , \tag{4.5}$$

where M_1 and M_2 are the masses of the parent and the daughter respectively. The leptonic current on the other hand retains its simple form for point

particles,

$$\langle\beta|l_\mu^W|\alpha\rangle = \bar{\psi}_e(p_e)\gamma^\mu(1+\gamma^5)\psi_\nu(p_\nu) \ , \tag{4.6}$$

where p_e and p_ν are the lepton 4-momenta.

The form factors g_V and g_A are vector and axial-vector, such that, in the zero-momentum transfer limit $g_V(q^2 \to 0) = c_V$ and $g_A(q^2 \to 0) = c_A$, mentioned in chapter 3. All the other terms are induced by the strong interaction in the decay process. g_M is called the 'weak magnetism' form factor, while g_T, g_S and g_P are the induced scalar, tensor and pseudoscalar form factors respectively, depending on their transformation properties. Holstein [24] generalized Eqn. (4.3) for any nuclear β decay (Fermi or Gamow-Teller) for $\Delta J = 0, \ \pm \ 1$ and $\Delta\pi =$ no, to obtain the induced hadronic form factors for nuclear transitions,

$$\begin{aligned} a &= g_V & c &= \sqrt{3}g_A \\ b &= \sqrt{3}g_M & d &= \sqrt{3}g_T \\ e &= g_S & h &= \sqrt{3}g_P \ . \end{aligned} \tag{4.7}$$

On using the CVC hypothesis one can obtain useful information about the form factors shown above. Direct comparison with the electromagnetic form factors yields $e = g_S = 0$. Therefore, if the CVC were true there would be no induced scalar currents. One can ignore the pseudoscalar term as it vanishes in the non-relativistic limit and we are left with only the a, b, c and d form factors. In the limit $q^2 \to 0$, the first two take the form

$$a(0) = [(T \mp T_z)(T \pm T_z + 1)]^{1/2} \tag{4.8}$$

$$b(0) = a(0)\left(\frac{J+1}{J}\right)^{1/2}(\mu_\beta - \mu_\alpha) \ , \tag{4.9}$$

where $\mu_{\alpha,\beta}$ are the nuclear magnetic moments and $a(0)$ is the familiar Fermi matrix element. The weak magnetism form factor $b = \sqrt{3}g_M$ is a higher-order induced term that is permitted in the standard model and manifests itself when the allowed approximation for β decays breaks down. It plays a significant role at higher momentum transfers. Murray Gell-Mann [23]

suggested experiments to measure the weak magnetism in nuclear β decays. He used the CVC hypothesis to conclude that the weak magnetism effect in β decays was analogous to the magnetic effects that induce dipole radiation in electromagnetism. The weak magnetism matrix element can in principle be extracted from the measured width of an analog $M1$ transition [23].

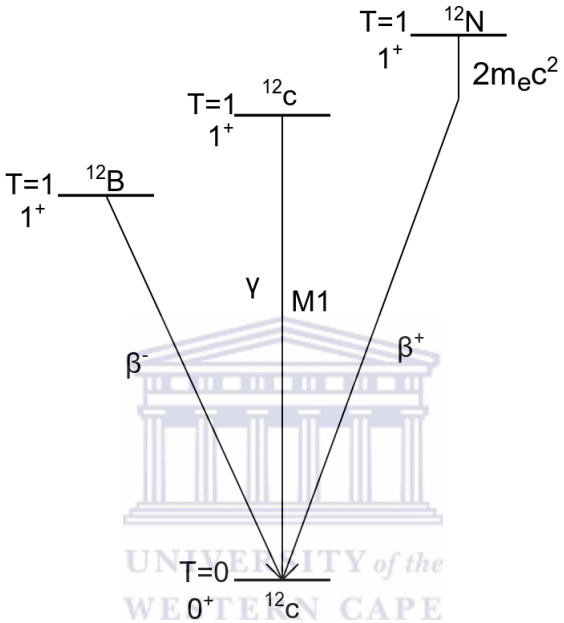

Figure 4.2: The CVC test in the $A = 12$, $T = 1$ triplet. One can extract the weak magnetism form factor for the Gamow-Teller decays via a measurement of the $M1$ width, Γ_{M1}.

In particular, Gell-Mann suggested measurements in the $T = 1$, $A = 12$ triad (shown in Fig. 4.2) where the decay Q value is rather large, ensuring a large momentum transfer. He derived the relation between b and Γ_{M1}, assuming the CVC hypothesis

$$b = \left(\frac{\Gamma_{M1}.6M^2}{\alpha E_\gamma^3}\right)^{1/2} , \tag{4.10}$$

where E_γ is the γ-ray energy, α is the fine structure constant and M is the same as in Eqn. (4.5) .

4.3 The induced tensor and second-class currents

The higher-order induced terms in the transition amplitude (4.4) lead to a $\ell > 0$ orbital momentum contribution from the leptonic wavefunction. Thus, the allowed approximation described in Section 2.1 is no longer valid. The other induced term apart from the weak magnetism, the tensor term $d = \sqrt{3}g_T$ is not included in the weak interaction structure of the standard model on the basis of certain symmetry arguments. One such important symmetry is called 'G-parity'. The G-parity operation is basically the product of a charge-conjugation operator C and a rotation by 180° about the second axis in isospin space,

$$G = Ce^{i\pi T_y} \ . \tag{4.11}$$

G-parity operations are invariant in the strong interaction. Since nuclear β decays involve strongly interacting quarks, one can split the weak interaction current into two classes depending on their transformation properties under G-parity. 'First-class' currents are defined under a G-parity transformation as ones that do not change sign

$$\begin{aligned} GV_\mu G^{-1} &= V_\mu \\ GA_\mu G^{-1} &= -A_\mu \ , \end{aligned} \tag{4.12}$$

while 'second-class' currents behave in an opposite manner and change sign

$$\begin{aligned} GV_\mu G^{-1} &= -V_\mu \\ GA_\mu G^{-1} &= A_\mu \ . \end{aligned} \tag{4.13}$$

Within the standard (quark) model, the symmetry demands that second-class currents do not exist [25]. However there is no fundamental reason why this should be so. Nuclear beta decay form factors can have both first class and second class components. For transitions within a common isospin multiplet, in the limit of good isospin symmetry, the d form factor ought to vanish in the presence of purely first-class currents. Thus, if a large non-zero d term were measured, this can only be due to a second-class contribution.

Since the induced terms under consideration d (induced tensor) and b (weak magnetism) both lead to $\ell > 0$ contributions in the β decay process, one can measure angular correlations in β decays to experimentally search for second-class tensor interactions [21]. One such angular correlation is the $\beta - \gamma$ correlation, which ought to be isotropic in the presence of only the $\ell = 0$ part of the leptonic current. Any anisotropy in the correlation would be due to both b and d terms in the decay.

4.4 Gammasphere experiment - The $\beta - \gamma$ directional correlation on ^{22}Na decay

The β decay of ^{22}Na offers an attractive possibility to search for second-class currents due to two reasons:

1. As shown in Fig. 4.3, the β decay is a $\Delta J = 1$, Gamow-Teller type, with a relatively large log ft value of 7.42 [3].

2. The ^{22}Na nuclide is a readily available source, with $T_{1/2} = 2.6$ yr, making it easy to use experimentally, without an accelerated beam.

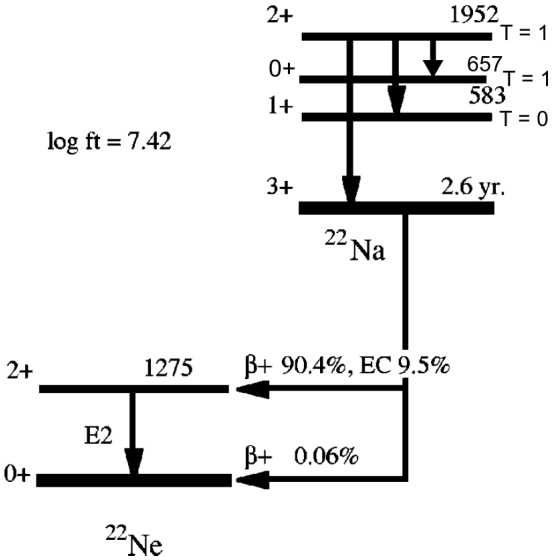

Figure 4.3: Decay scheme of ^{22}Na, the energies are in keV.

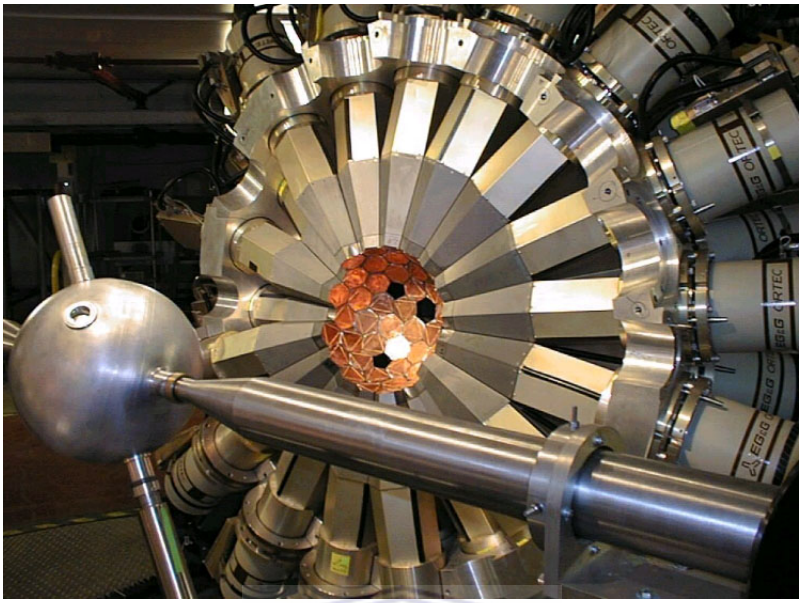

Figure 4.4: Gammasphere array at the Lawrence Berkeley National Laboratory

The large ft value mentioned above indicates a highly suppressed allowed matrix element which increases the experimental sensitivity to the higher-order matrix elements, particularly, the weak magnetism and the second-class tensor terms. Therefore, a measured $\beta - \gamma$ directional correlation in this decay could show more of an anisotropy compared to other cases where the allowed Gamow-Teller matrix element dominates. Taking advantage of these facts, an experiment was carried out by Bowers *et al.* [3] at the Lawrence Berkeley National Laboratory using Gammasphere, an array of 100 Compton suppressed Germanium detectors, shown in Fig. 4.4. The purpose of the experiment was to measure the angular correlation between an emitted β particle (corresponding to the $3^+ \rightarrow 2^+$ β transition) and the $2^+ \rightarrow 0^+$, $E_\gamma = 1275$ keV photon in the ^{22}Ne daughter. Both these transitions are shown in in Fig. 4.3.

In the experiment, a 6 μCi ^{22}Na source and a 3 mm-thick plastic scintillator detector were placed in the center of the array over 9 days of beam shut down period. For each Germanium detector, coincident $\beta - \gamma$ events and γ singles

events were collected over this time period. As shown in Fig. 4.5, the experiment yielded a non-zero $\beta-\gamma$ directional coefficient of $A_{22} = 0.53(25) \times 10^{-3}$. A comparison of this result with previous work is shown in Fig. 4.6. This result differed significantly from earlier work that was reported with comparable precision.

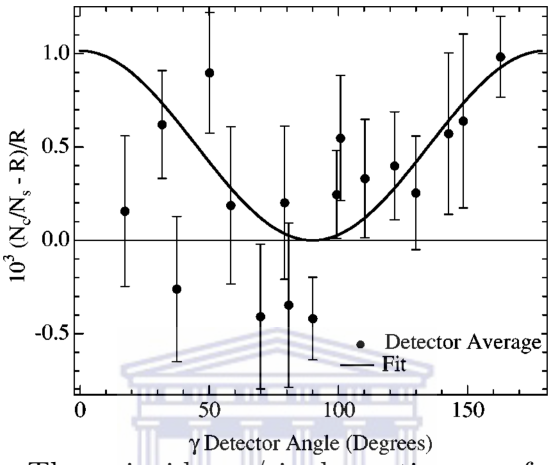

Figure 4.5: The coincidence/singles ratio as a function a γ detector angle from [3].

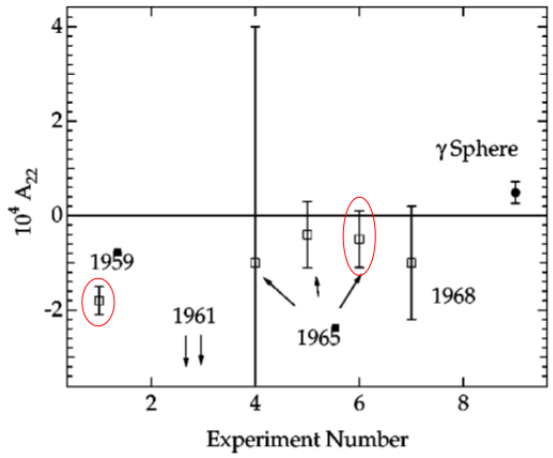

Figure 4.6: Comparison of the Gammasphere result to the previous measurements [26, 28, 29, 30, 31]. The most precise earlier results are highlighted for comparison.

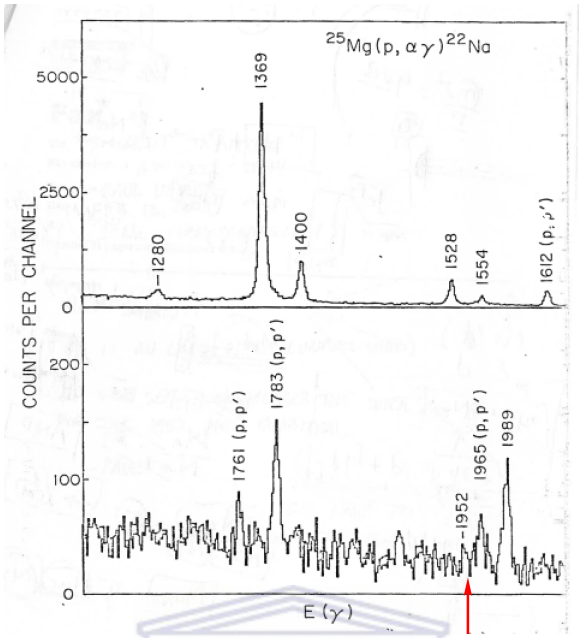

Figure 4.7: The MSU experiment spectrum from [2]. The location of the 1952 keV gamma-ray is shown.

The measured $\beta - \gamma$ directional coefficient relates to the induced form factors using a parametrization recommended by Firestone *et. al.* [32]

$$A_{22} = (4.4B + 4.4D - 0.6C_2) \times 10^{-5} \ , \tag{4.14}$$

with $B = b/Ac_1$, $D = d/Ac_1$, $C_2 = c_2/Rc_1$. In the above, R is the nuclear radius, A is nucleon number, c_1 is the Gamow-Teller coupling $g_A M_{GT}$ and c_2 is a higher-order axial-vector term that is a function of q^2 [32]. Assuming that $C_2 \approx 0$, Bowers *et. al.* extracted the weak magnetism using an unpublished value of the analog $2^+ \rightarrow 3^+$ gamma (M1) width from a previous ^{25}Mg$(p, \alpha\gamma)$ measurement at the Michigan State University (MSU) [2]. The spectrum from the MSU experiment is shown in Fig. 4.7. Together with their measured A_{22} coefficient, Bowers *et. al.* extract an unexpectedly large second-class tensor term, $D = 26(7)$ which disagrees with the Standard Model. This result also disagrees with other experiments that did not find conclusive evidence for second-class currents in $A = 12$ and $A = 20$ nuclei [21].

It is obvious from the above that the weak link in this work is the extraction of the weak magnetism b/Ac_1 from the spectrum shown in Fig. 4.7. The experimenters at MSU assumed the analog $1952 \rightarrow 0$ keV isovector transition shown in Fig. 4.3 to be purely $M1$ and disregarded the small $1952 \rightarrow 657$ keV $E2$ branch of 0.3% [33]. More importantly, although their experiment lacked the statistics to make any conclusive claims, the authors of Ref. [2] concluded that $\Gamma_{M1} = (3.6 \pm 1.7) \times 10^{-4}$ eV based on their extraction of $(0.61 \pm 0.24)\%$ for the $1952 \rightarrow 0$ keV analog branch.

This thesis describes an independent experiment to obtain the analog $M1$ branch for ^{22}Na decay in an attempt to explain the anomalously large d term measured for this particular decay. We describe the experimental procedure and the analysis in the following chapters.

Chapter 5

The ^{21}Ne(p,γ) experiment

In our experiment, the 2_1^+ state of interest in ^{22}Na was produced using the ^{21}Ne(p,γ) resonance reaction. In this chapter I first briefly explain resonances in nuclear reactions before getting into the experimental details.

5.1 Resonance reactions

Consider a beam of particles incident on a target. If the incident beam scatters off the target leaving it in the ground state then the interaction is referred to as elastic scattering. If the target nucleus changes as a result of the collision then a nuclear reaction is supposed to have taken place. The elastic scattering and reaction probabilities are given by their cross sections, as a sum of partial waves [34]

$$\sigma_{el} = \sum_{\ell=0}^{\infty} \sigma_{el,\ell} \qquad \text{and} \qquad \sigma_{re} = \sum_{\ell=0}^{\infty} \sigma_{re,\ell} \ . \tag{5.1}$$

A cross section uniquely depends on something called a phase shift, such that, in general for a given orbital angular momentum ℓ

$$\sigma = \frac{\pi}{k^2}(2\ell+1)\left|1 - e^{2i\delta_\ell}\right|^2 \ . \tag{5.2}$$

The phase shift δ_ℓ arises due to the scattering process off a given potential. The radial solutions to the Schrödinger equation for a quantum mechanical scattering problem are such that an incoming plane wave is shifted in phase relative to a free outgoing wave due to the influence of the potential.

Consider the scattering off a three-dimensional square-well attractive potential. The radial solutions to the Schrödinger equation for this problem are, for a radius R and depth V_0,

$$u_\ell^{\text{in}} = Ae^{iKr} + Be^{-iKr}, \qquad r < R \tag{5.3}$$

$$u_\ell^{\text{out}} = Ce^{ikr} + De^{-ikr}\ , \qquad r > R \tag{5.4}$$

where $K^2 = 2m(E + V_0)/\hbar^2$ and $k^2 = 2mE/\hbar^2$. The continuity conditions require that these wave functions and their derivatives are matched at the boundary,

$$\left(u_\ell^{\text{in}}\right)_R = \left(u_\ell^{\text{out}}\right)_R \tag{5.5}$$

$$\left(\frac{du_\ell^{\text{in}}}{dr}\right)_R = \left(\frac{du_\ell^{\text{out}}}{dr}\right)_R . \tag{5.6}$$

It is convenient to introduce a dimensionless quantity, called the logarithmic derivative at the boundary,

$$f_l \equiv R\left(\frac{1}{u_l(r)}\frac{du_l(r)}{dr}\right)_{r=R} = R\left(\frac{d}{dr}\ln u_l(r)\right)_{r=R}\ , \tag{5.7}$$

which helps one to rewrite the continuity conditions as,

$$f_l(u_\ell^{\text{in}}) = f_l(u_\ell^{\text{out}})\ . \tag{5.8}$$

In terms of the phase shift, the total outgoing wavefunction can be written as

$$u_\ell^{\text{out}}(r) = \frac{i}{2kr}\left(e^{-ikr} - e^{2i\delta_\ell}e^{ikr}\right)\ . \tag{5.9}$$

For $\ell = 0$ (s-wave) scattering, since the cross section is determined by the phase shift δ_0, one can find the relation between δ_0 and f_0 and express the cross section in terms of f_0. Substituting Eqn. (5.9) into (5.7) and solving for $e^{2i\delta_0}$ one gets,

$$e^{2i\delta_0} = \frac{f_0 + ikR}{f_0 - ikR}e^{2ikR}. \tag{5.10}$$

Further substituting in Eqn. (5.2), we get the cross section for s-wave elastic scattering

$$\sigma_{el} = \frac{\pi}{k^2}\left|\underbrace{-\frac{2ikR}{f_0 - ikR}}_{A_{res}} + \underbrace{e^{2ikR} - 1}_{A_{pot}}\right|^2 \tag{5.11}$$

with a 'resonant' scattering amplitude (A_{res}) and a potential scattering amplitude (A_{pot}). The resonant term corresponds to a large amplitude in the cross section at the interior of the potential well, so that the slope of the radial wave function vanishes at $r = R$.

Now, consider a s-wave scattering such that there is a phase difference of ζ between the incoming (e^{-iKr}) and outgoing (e^{iKr}) waves. With the assumption that that the amplitude of the incoming wave, e^{-iKr} is $A = Be^{2i\zeta}e^{2q}$ (where ζ and q are real numbers), one can reduce Eqn. (5.3) to the following form

$$u_{\text{in}} = 2Be^{(i\zeta - q)}\cos(Kr + \zeta + iq)\ , \tag{5.12}$$

where the logarithmic derivative for this problem is

$$f_0 = -KR\tan(KR + \zeta + iq)\ . \tag{5.13}$$

The idea is to express the cross sections near a single resonance in terms of the measurable quantities. One can define resonance energies, E_r by the condition that f_0 vanishes at these energies to give a large cross section

$$f_0(E_r, q) = -KR\tan(KR + \zeta + iq) = 0\ . \tag{5.14}$$

$f_0(E_r, q)$ can be Taylor expanded about the resonance E_r, with $q = 0$ to give

$$f_0 \simeq f_0(E_r, q) + (E - E_r)\left(\frac{\partial f_0}{\partial E}\right)_{E_r, q=0} + q\left(\frac{\partial f_0}{\partial q}\right)_{E_r, q=0} \cdots\ , \tag{5.15}$$

so that

$$f_0 \simeq (E - E_r)\left(\frac{\partial f_0}{\partial E}\right)_{E_r, q=0} - iqKR\ . \tag{5.16}$$

Substitution of Eqn. (5.16) into Eqn. (5.11) leads to the following definitions [34, 35]

$$\Gamma_a = -\frac{2kR}{(\partial f_0/\partial E)_{E_r,q=0}} \qquad \text{(particle width)}$$

$$\Gamma_r = -\frac{2qKR}{(\partial f_0/\partial E)_{E_r,q=0}} \qquad \text{(reaction width)}$$

$$\Gamma = \Gamma_a + \Gamma_r \ , \qquad \text{(total width)}$$

so that the total cross section is (from Eqn. (5.11)),

$$\sigma = \frac{\pi}{k^2}\left|\underbrace{\frac{i\Gamma_a}{(E-E_r)+i\Gamma/2}}_{A_{res}} + \underbrace{e^{2ikR}-1}_{A_{pot}}\right|^2 \ , \tag{5.17}$$

with the resonant component of the cross section being

$$\sigma = \frac{\pi}{k^2}\frac{\Gamma_a^2}{(E-E_r)^2+\Gamma^2/4} \ . \tag{5.18}$$

This is called the Breit-Wigner formula for resonant elastic scattering of spinless particles.

In general, if we consider the spin of the particles involved in a reaction and the total angular momentum of the resonant state which has a decay width Γ_b, the resonant cross section is given by,

$$\sigma = \frac{\pi}{k^2}\frac{\Gamma_a\Gamma_b}{(E-E_r)^2+\Gamma^2/4}\cdot\frac{(2J+1)}{(2J_1+1)(2J_2+1)} \ , \tag{5.19}$$

where J is the angular momentum of the resonant state, J_1 and J_2 are the spins of the projectile and target nuclei respectively. Following the arguments stated before, the cross section for this particular reaction channel is enhanced when the incident beam energy is close to the resonance energy E_r.

5.2 Target preparation and Experimental facility

The selectivity and large cross section of producing particular states using resonance reactions was used as a motivation to produce the first 2^+ state

in ^{22}Na using the ^{21}Ne(p,γ) reaction. However, since the ^{21}Ne nuclide is naturally available a gas and has low abundance (0.27%), it was decided to use an implanted ^{21}Ne target. The target was prepared at the Center for Experimental Nuclear Physics and Astrophysics (CENPA) at the University of Washington in Seattle, USA. A 30 keV, 50 pnA ^{21}Ne^{++} beam from a modified Direct Extraction Ion Source (DEIS) at this facility was mass separated through a 90° bending magnet and implanted on to a 1-mm-thick 99.9% pure Tantalum backing over a period of several days. The beam was rastered using magnetic steerers, so that a uniform implantation region of a diameter 1 cm produced the required target with a thickness of $\approx 13\ \mu g/\text{cm}^2$. The ion source is shown in Fig. 5.3. The tandem facility at the University of Washington (shown in Fig. 5.1) was also modified so that the accelerator could be used as a single-ended machine with a positive (RF) ion-source placed at the terminal. This ensured a high proton beam intensity at low energies.

Figure 5.1: The tandem accelerator facility at CENPA.

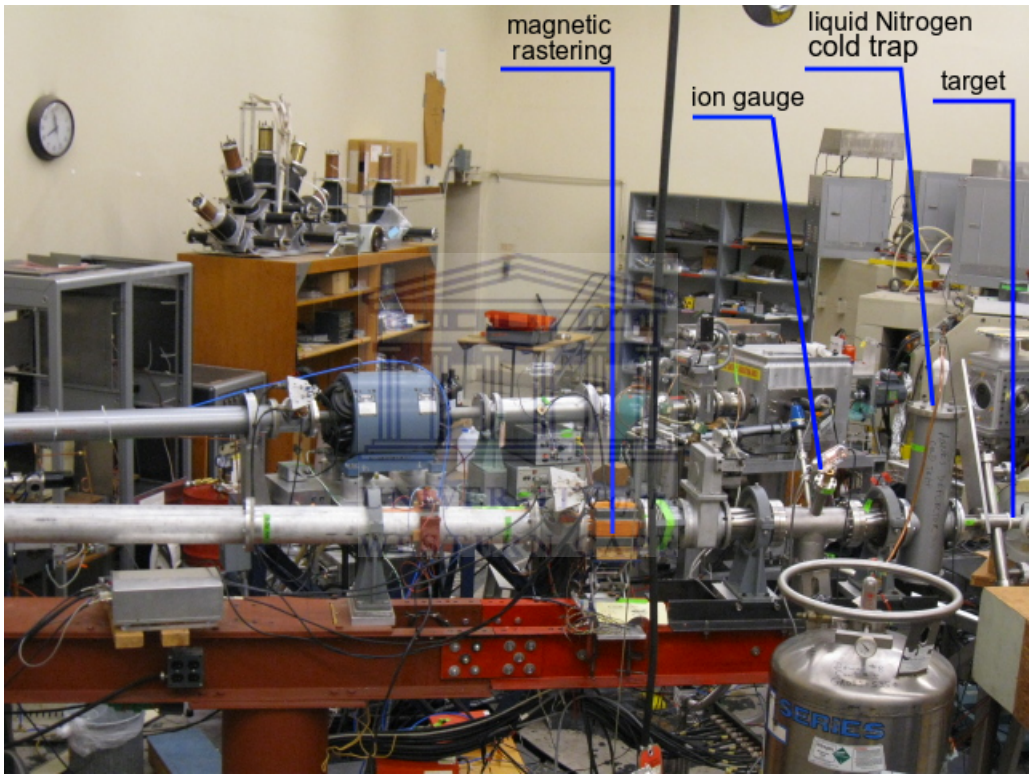

Figure 5.2: The 30° beam line at CENPA.

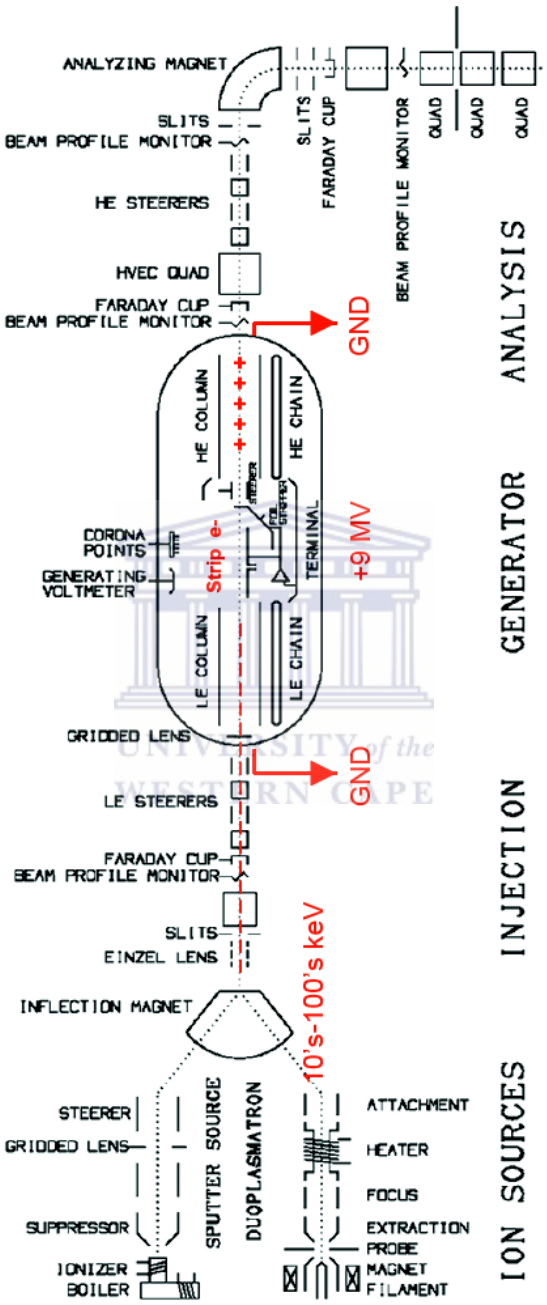

Figure 5.3: CENPA Tandem accelerator

For this experiment it was decided to use a resonance at proton energy $E_p = 1113$ keV, which almost exclusively produces a state in ^{22}Na at 7800 keV [36].

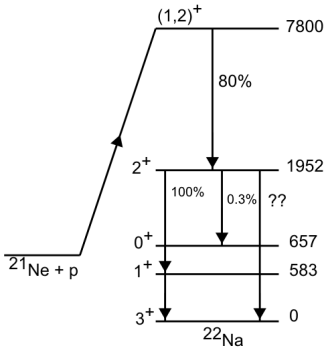

Figure 5.4: The ^{21}Ne(p,γ) resonance and gamma-rays of interest. Energies are in keV. The $1952 \rightarrow 0$ branch is not listed in the NNDC database [33].

As shown in Fig. 5.4, this state feeds the 2_1^+ state of interest with a branching ratio of 80% [36], which further decays predominantly to the 1^+ state at 583 keV, thereby emitting a gamma-ray at energy $E_\gamma = 1369$ keV [33].

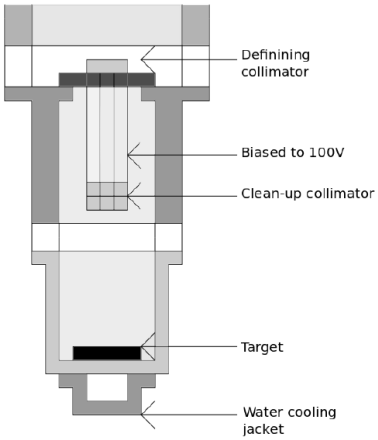

Figure 5.5: Schematic of the target station at the 30° beam line at CENPA.

The target was mounted on the 30° beam line at CENPA which is shown in Fig. 5.2. A schematic of the target chamber is shown in Fig. 5.5. A 60μA proton beam with energy $E_p = 1113$ keV was sent through a set of collimators with electrical suppression (to prevent delta electrons) and bombarded the ^{21}Ne implanted Tantalum backing that had water cooling on its back. The cooling minimized damage to the target due to the power deposited by the high intensity beam. Furthermore, the proton beam was rastered over an area of ≈ 0.2 cm^2 using an alternating magnetic field to prevent local heating at the beam spot. Three detectors were used to register the gamma-rays that were emitted from the reaction. One large $10'' \times 15''$ NaI detector was used to collect coincidences by gating on the 5848 keV gamma-ray from the 7800 $\rightarrow$ 1952 keV transition, while two 100% N-type Canberra HPGe detectors were used to collect gamma-ray information from the subsequent transitions. The data were collected with the detectors in two configurations shown in Figs. 5.6 and 5.7.

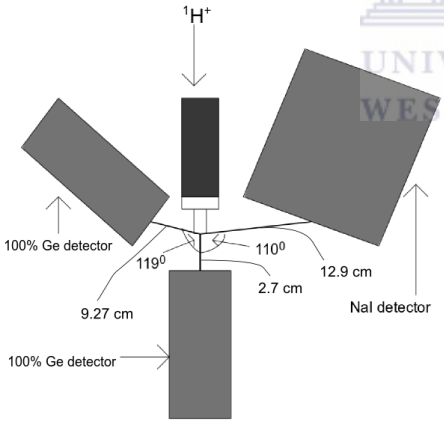

Figure 5.6: Schematic setup for the detector geometry in the close packed configuration.

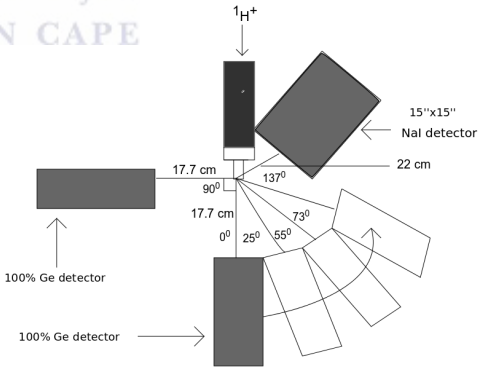

Figure 5.7: Schematic of detector configuration for the second data set.

In the first configuration, the Germanium detectors were close-packed, for a branching ratio measurement. In the second configuration, the Germanium

detetors were moved away from the target, with one detector kept fixed at 90° to the beam, while the other was used to take data at different angles to get an angular distribution. In the former, 2.54-cm-thick lead bricks were placed in front of the HPGe detectors, while in the second, 1.2-cm-thick lead bricks were placed on the face of the detectors. This ensured that there was negligible summing of the 1952 → 583 → 0 keV cascades in the detectors.

5.3 Data Acquisition

The signal from the detectors were shaped using a previously set up data acquisition system described in Ref. [37]. The HPGe signals were amplified and sent to a ORTEC 413A ADC with a FERA read-out for digitization on a computer via a CAMAC crate. A java based data acquisition called JAM was used for processing and online analysis of the data [38]. The signals from the Germanium detectors and the NaI detector were further used as start-stop inputs to ORTEC566 Time-to-Amplitude convertors (TAC's) to collect coincidences. γ-ray singles data were also registered simultaneously.

Chapter 6

Analysis and Monte Carlo Simulations

During the ^{21}Ne(p,γ) experiment we took data for 3 days in the close-packed configuration and for roughly 7 days with the detectors further away to obtain angular distribution information. In this chapter I describe the procedure used to analyze these data.

6.1 Energy calibration

The energy calibration for the detectors was performed using ^{56}Co and ^{60}Co gamma-ray sources. The activity of the ^{60}Co source ($T_{1/2}$ = 5.27 yr) was known from the manufacturer to be A_0 = 1.812 kBq on December 15, 2005. This source emitted two γ-rays with well known energies E_{γ_1} = 1173.228 keV and E_{γ_2} = 1332.492 keV. The ^{56}Co source of unknown activity emitted well known γ-rays in the energy range 846 $\leq E_\gamma \leq$ 3451 keV. To perform the energy calibration, the peaks in all γ-spectra were fit using a function that included a Gaussian

$$G(x) = \frac{1}{\sqrt{2\pi\sigma^2}} exp(\frac{-(x-\mu)^2}{2\sigma^2}) \ , \tag{6.1}$$

and a lineshape of the form

$$T(x,\mu) = \frac{1}{2l} exp\Big[\frac{(x-\mu)}{l} + \frac{1}{2}\Big(\frac{\sigma}{l}\Big)\Big] erfc\Big[\frac{1}{\sqrt{2}}\Big(\frac{(x-\mu)}{\sigma} + \frac{\sigma}{l}\Big)\Big] \ , \tag{6.2}$$

which arises from a convolution of a Gaussian with a low energy exponential tail. In the above, erfc is the complementary error function, l is the decay length of the exponential tail, μ is the peak centroid and σ, the standard deviation is related to the full-width half-maximum (FWHM) of a pure Gaussian, such that FWHM $= 2\sqrt{2\ln 2}\sigma$. The fitted centroids were used for an energy calibration using a linear regression [39],

$$E_\gamma(i) = a_0 + a_1\mu(i) \ , \tag{6.3}$$

where $\mu(i)$ represents the fitted centroid of a i^{th} gamma-ray up to 3.2 MeV. The regression yielded the following calibration coefficients shown in the table below. The calibrated energy spectra of both sources from HPGe1 are shown in Fig. 6.1. A sample fit and its residuals are shown in Fig. 6.2.

Table 6.1: Energy calibration coefficients for the three detectors. The uncertainties in the coefficients are not shown

Detector*	a_0	a_1
HPGe 1	10.07	1.08193
HPGe 2	7.29	1.08471
NaI	87.1	1.331573

*HPGe1 was used as the 0° detector for all the measurements described in this chapter.

6.2 Dead time corrections (for efficiency calibration).

The next step in the analysis was an efficiency calibration of the detectors. For an accurate calibration dead time corrections had to be performed. The concept of dead time and its correction procedure is explained below.

The events from the detectors are recorded as pulses in the data acquisition system. When the pulses get analyzed by the data acquisition system, successively registered events are separated by a minimum time called the

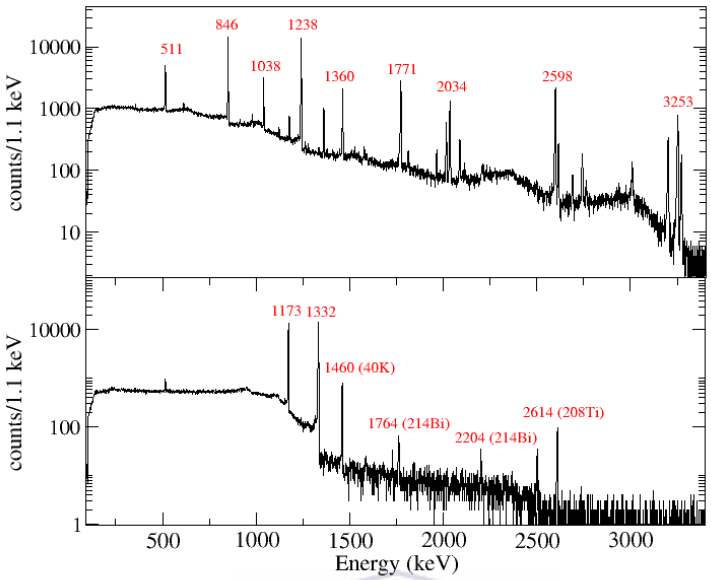

Figure 6.1: Energy calibrated energy γ-ray singles spectra for the ^{56}Co and ^{60}Co sources from one of the detectors. Only the prominent peaks from both sources and room background are labeled. The pulser peak is outside the range in these histograms and not shown.

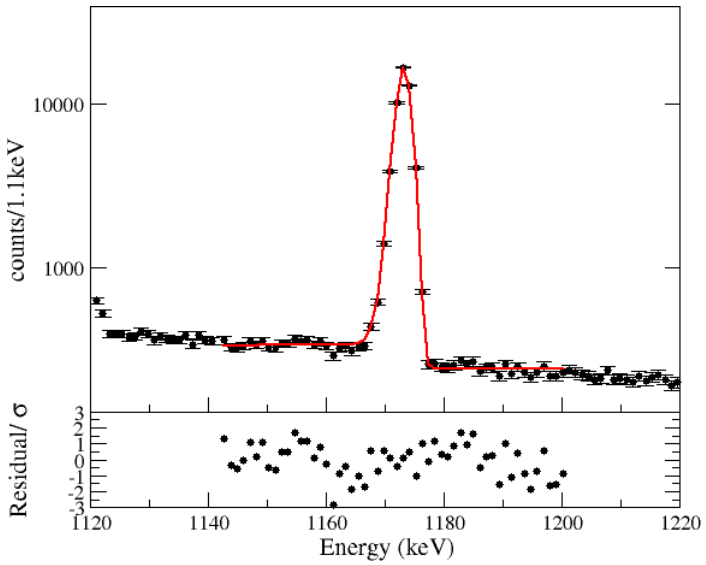

Figure 6.2: A sample fit to the 1173 keV peak.

'dead time' that is required to process the signal from the first pulse. Therefore while analyzing data from detector systems, one has to take into account the effect of dead time loss for absolute measurements. For a given true event rate n, the recorded rate m in a detection system is given by,

$$m = n(1 - m\tau) \ , \tag{6.4}$$

where τ is the non-extendible dead time for each event. The product $m\tau$ gives the fraction of the events lost due to the dead time of the system.

It should be noted here that for the $^{21}\mathrm{Ne}(p,\gamma)$ experiment, our data acquisition was triggering at relatively low rates (maximum of $\sim$ 400 Hz) ensuring a low effective dead time. Nonetheless, in order to determine the efficiencies of the HPGe detectors accurately, we performed dead time corrections. For these corrections, a Berkeley Nucleonics high-precision pulser was used to send signals at a rate of 100 Hz to a scalar unit on the CAMAC crate. This signal was split and simultaneously sent into the preamplifier input of one Germanium detector. The ratio of the total number of pulser counts registered by the scalar to the total pulser counts in the HPGe detector spectrum gave us the fraction of events lost due to the dead time in each run,

$$f_d = 1 - \frac{N_d}{N_s} \ , \tag{6.5}$$

where N_s and N_d are the pulser counts from the scalar and detector spectrum respectively. Note that Eqn. (6.5) is similar to the product $m\tau$ in Eqn. (6.4). The fraction N_d/N_s is the fraction of counts registered in the 'live time', denoted by f_l. Using the fitted ^{56}Co and ^{60}Co peaks, together with f_l, the dead-time-corrected photo peak areas were calculated using the ratio

$$N_\gamma(i) = \frac{N_{\mathrm{peak}}(i)}{f_l} \ . \tag{6.6}$$

6.3 Efficiency calibration

The dead-time-corrected peak areas were used to get the efficiencies of the Germanium detectors in different configurations. Using the data from the

^{60}Co source, we obtained the absolute efficiencies of the detectors using the relation

$$\epsilon_{\gamma}^{abs}(i) = \frac{N_{\gamma}(i)}{AI_{\gamma}(i)t} \ , \tag{6.7}$$

where A is the activity of the ^{60}Co source on the day of calibration, I_{γ} is the intensity of the γ-ray and t is the run time. The absolute efficiencies of the detectors for the ^{60}Co gamma rays are shown in Tables. 6.2 and 6.3. Since the absolute activity of the ^{56}Co source was not known, only the relative efficiencies of the detectors were obtained for the ^{56}Co gamma rays using the formula

$$\epsilon_{\gamma}^{Rel}(i) = \frac{N_{\gamma}(i)}{I_{\gamma}(i)} \ , \tag{6.8}$$

where $I_{\gamma}(i)$ are intensities of the γ-rays from the NNDC website [33]. These relative efficiencies were fit to a polynomial of the form

$$\ln\epsilon_{\gamma_{fit}}(i) = \sum_{j=0}^{3} a_j [\ln E_{\gamma}(i)]^j \ , \tag{6.9}$$

where $E_{\gamma}(i)$ represents the energy of the i^{th} γ-ray and the a_j's are the coefficients of the polynomial and are free parameters. One can then define, for N data points

$$\chi^2 = \sum_{i=1}^{N} \frac{1}{\sigma_i^2} \left[\ln\epsilon_{\gamma}(i) - \ln\epsilon_{\gamma_{fit}}(i)\right]^2 \ . \tag{6.10}$$

This χ^2 was minimized with respect to each parameter, such at

$$\frac{\partial}{\partial a_j}\chi^2 = 0 \ , \tag{6.11}$$

yielding a system of four linear equations. These were solved to obtain the coefficients a_j using the Gauss-Jordan elimination method [39, 40]. The fits to the relative efficiencies were finally normalized to absolute values using the ^{60}Co data and an independent least squares fitting algorithm, which converted the $\epsilon_{\gamma}^{Rel}(i)$ to $\epsilon_{\gamma}^{Abs}(i)$ for gamma ray energies up to 3.2 MeV. The absolute normalized efficiencies for the ^{56}Co lines are also shown in Tables 6.2 and 6.3. The quoted uncertainties are purely statistical. An estimation of the systematic effects by moving the source around, showed no significant effect. The fits are shown in the figures that follow.

Table 6.2: Absolute efficiencies for the HPGe detectors in the 'close pack' configuration.

Energy	I_γ %	$\epsilon_\gamma \times 10^3$	
		0°	119°
846.77	100	1.338(16)	0.743(11)
977.372	1.422(6)	1.416(167)	0.776(139)
1037.843	14.06(4)	1.798(66)	1.018(30)
1173.228	99.85(3)	2.029(61)	1.111(34)
1332.492	99.9826(6)	2.215(67)	1.197(36)
1360.212	4.286(12)	2.206(64)	1.228(52)
2015.215	3.018(12)	2.386(70)	1.201(4.9)
2034.791	7.774(28)	2.231(44)	1.216(31)
2598.5	16.98(4)	1.966(30)	1.100(21)
3202.029	3.211(12)	1.781(51)	0.993(37)
3253.503	7.928(21)	1.679(33)	0.881(23)
3273.079	1.877(2)	1.657(62)	0.959(46)

Table 6.3: Absolute efficiencies for the HPGe detectors for the 'angular distribution' configuration.

Energy	I_γ %	$\epsilon_\gamma \times 10^3$				
		$0°$	$-25°$	$-55°$	$-73°$	$90°$
846.77	100	0.786(39)	0.779(28)	0.572(16)	0.385(35)	0.612(23)
977.372	1.422(6)	0.749(294)	0.780(254)	0.608(148)	0.421(142)	0.680(163)
1037.843	14.06(4)	0.830(52)	0.846(41)	0.637(77)	0.455(35)	0.674(58)
1173.228	99.85(3)	0.851(117)	0.858(187)	0.660(207)	0.483(75)	0.701(225)
1332.492	99.9826(6)	0.856(117)	0.861(188)	0.678(212)	0.501(77)	0.719(229)
1360.212	4.286(12)	0.849(87)	0.849(63)	0.676(43)	0.498(48)	0.719(60)
2015.215	3.018(12)	0.756(79)	0.760(62)	0.628(45)	0.501(52)	0.647(61)
2034.791	7.774(28)	0.742(52)	0.747(40)	0.620(72)	0.497(77)	0.648(40)
2598.5	16.98(4)	0.635(36)	0.636(28)	0.543(46)	0.440(53)	0.563(28)
3202.029	3.211(12)	0.539(59)	0.535(45)	0.465(75)	0.381(39)	0.476(46)
3253.503	7.928(21)	0.533(39)	0.535(31)	0.459(23)	0.378(68)	0.479(31)
3273.079	1.877(2)	0.5300(73)	0.524(56)	0.453(42)	0.377(48)	0.484(58)

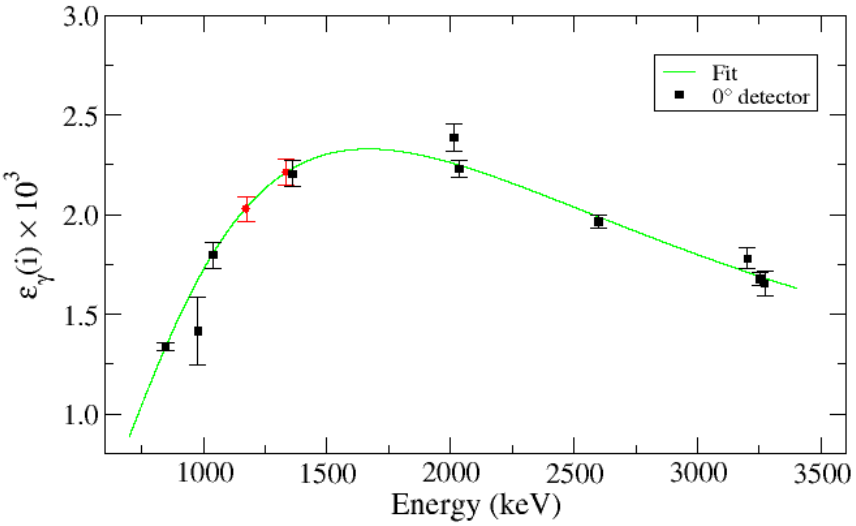

Figure 6.3: Experimentally determined efficiencies for HPGe1 at 0° in the close-packed configuration. The ^{60}Co values are highlighted in red.

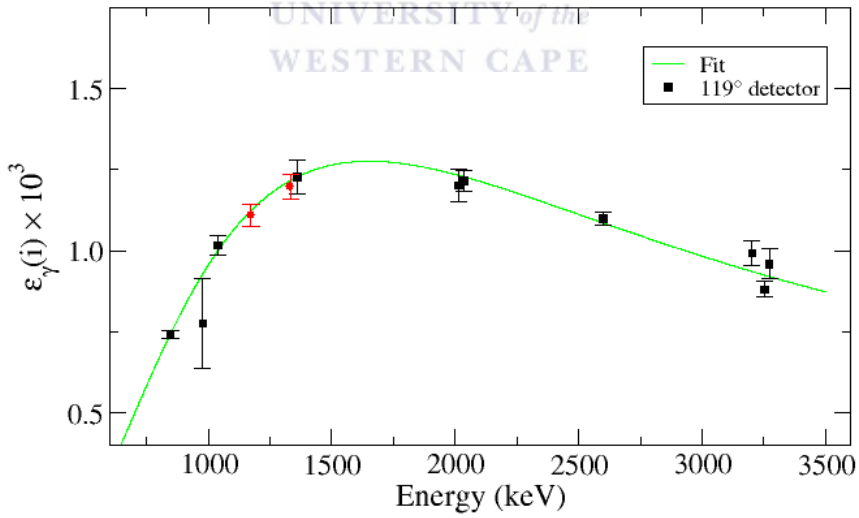

Figure 6.4: Experimentally determined efficiencies for HPGe2 at 119° in the close-packed configuration. The ^{60}Co values are highlighted in red.

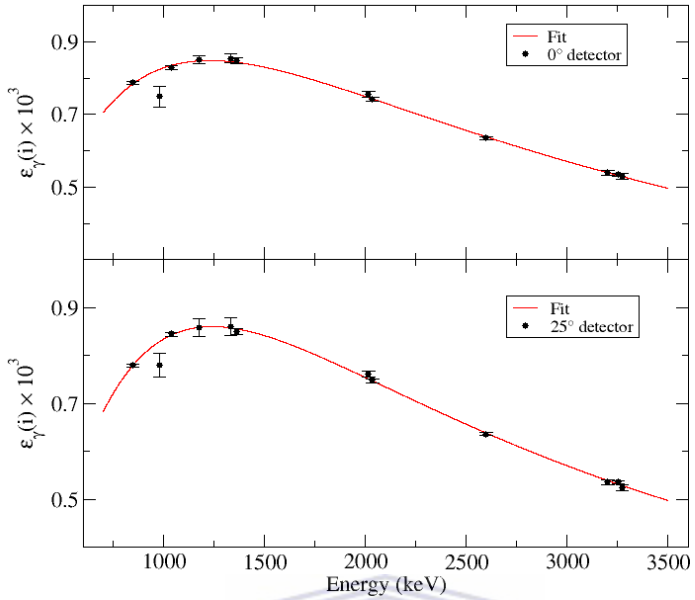

Figure 6.5: Experimentally determined efficiencies for HPGe1 at 0° and 25° in the second configuration.

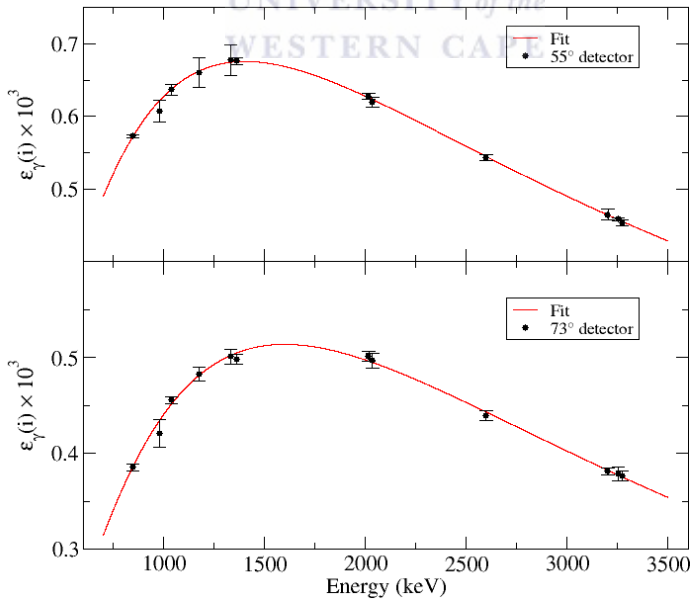

Figure 6.6: Experimentally determined efficiencies for HPGe1 at 55° and 73° in the second configuration.

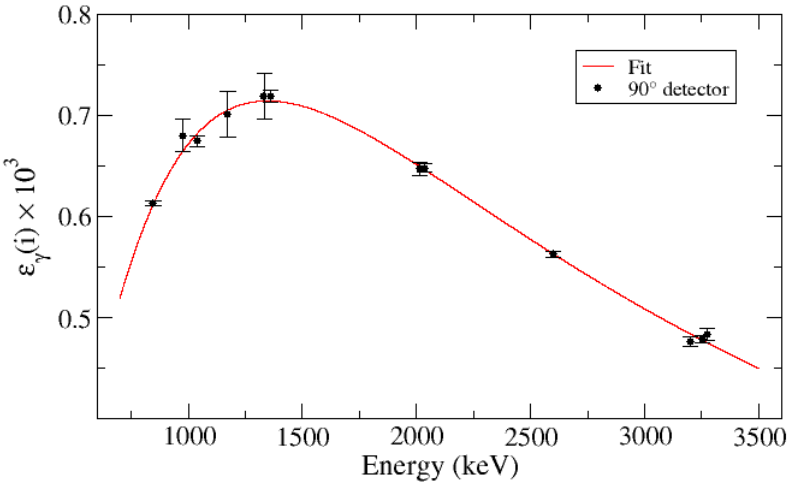

Figure 6.7: Experimentally determined efficiencies for HPGe2 at 90° in the second configuration.

Once the experimental γ-ray detection efficiencies were obtained, we proceeded to perform several Monte Carlo simulations for the following reasons:

1. To correct for the attenuation of the gamma-rays due to the water cooling. This is because the water cooling was not on while taking calibration data.

2. To obtain corrections due to photon summing and scattering for a precise branching ratio measurement.

3. To study the effects of source distribution and γ-ray multipolarity for our measurement.

4. To secure our understanding of the detector geometry (particularly the distance and the angle relative to the beam spot) rather than relying on mechanical measurements which were prone to errors in our 'table-top' arrangement.

In particular, it should be noted with regard to the final point above, as it was not planned beforehand to take the angular distribution data, the second data set was obtained using a make-shift arrangement of a table and a

support structure on wheels that allowed us to rotate one germanium detector (HPGe1) about the beam axis. Therefore, a crucial step in the analysis was to precisely understand the geometry, particularly of the second setup using Monte Carlo simulations. The crystal specifications that were supplied by the manufacturer were already stringently tested and determined previously using a rigorous method that employed Monte Carlo simulations together with source data [41]. We performed several additional simulations similarly to optimize our knowledge of the detector geometry. These simulations are described below.

6.4 PENELOPE Simulations

PENELOPE (Penetration and ENErgy LOss of Positrons and Electrons) is a radiation transport FORTRAN computer code that is used to perform Monte Carlo simulations of electron, positron and photon transport in materials over a large energy range [42]. The PENELOPE package was employed in this work because of its efficiency and accuracy to model radiation transport problems [43, 44].

For the simulations, the detectors and target-ladder arrangement were constructed in a solid geometry model as objects that are defined by the volume enclosed between a set of quadric surfaces. Figures 6.8 and 6.9 show a 3-dimensional view of the experimental set up built for the simulations. Figure 6.10 shows a zoomed-in picture of the copper target holder and aluminum water cooling jacket.

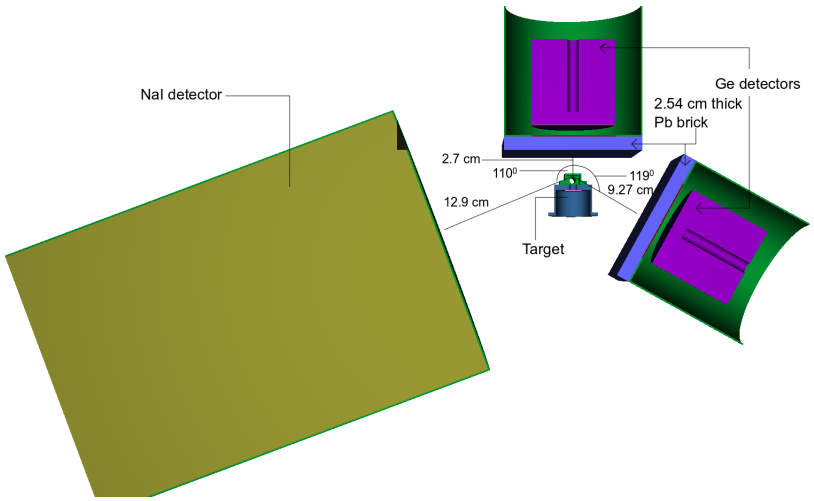

Figure 6.8: Close-pack configuration: Cross sectional view of two Ge detectors and the NaI detector. The target holder with the Al water cooling jacket are shown.

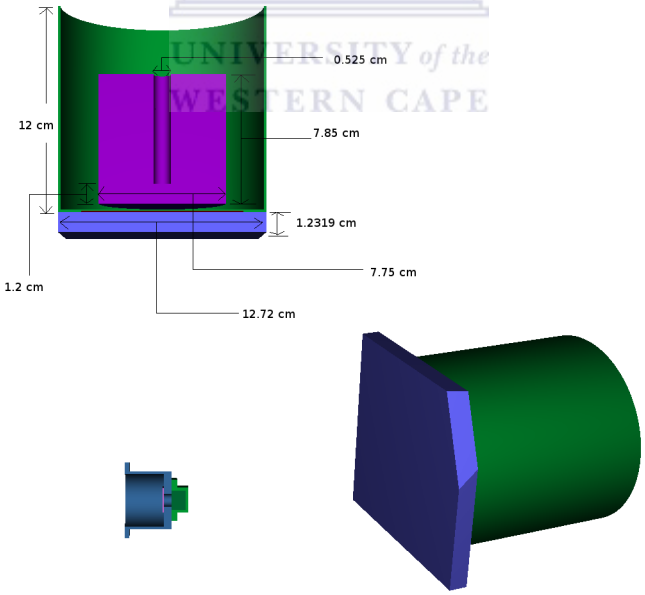

Figure 6.9: One configuration used for angular distribution measurement. Note that the NaI detector was moved further away for this measurement and is not visible in this picture.

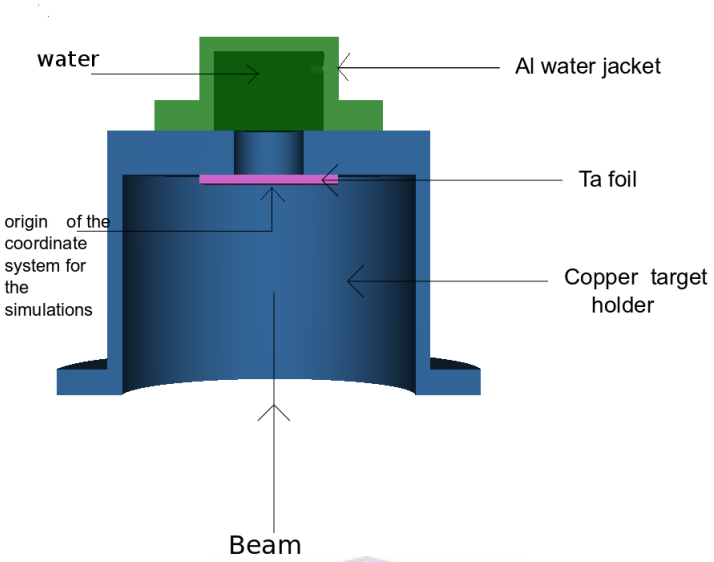

Figure 6.10: The target holder and water cooling jacket in the model.

To optimize the positions of the HPGe detectors, starting with the 'nominal' measured values, several combinations of detector angle and distance were used to generate histograms for the ^{56}Co and ^{60}Co gamma-rays from the simulations. In the simulations, monoenergetic γ-rays were emitted isotropically from the center of the Tantalum foil (shown in Figure 6.10) in the energy range 846< E_γ <3273 keV. The simulated efficiencies were then compared to the experimental values shown in Tables 6.2 and 6.3. We defined a $\chi^2 = \left(\frac{\epsilon_{\rm sim}(i)-\epsilon_{\rm data}(i)}{\Delta\epsilon_{\rm data}(i)}\right)^2$ to obtain the optimal parameters for a given simulation. Several simulations we performed with small variations in the values of the detector distance and angle to obtain the optimal geometry that yielded the minimum χ^2 mentioned above. A comparison of the simulated results for the 'best geometries' with the experimental curves is shown in the figures and tables below [1].

[1]In our simulations, we used 10^6 photon emissions for each gamma ray in the close-packed geometry and 16×10^6 photons for each gamma ray in the 'angular distribution' geometry.

Table 6.4: Comparison between the measured and simulation-determined parameters for the close-packed configuration.

Nominal θ_{detector}	Target-detector distance (cm)	θ_{detector} inferred from simulations	Target-detector distance from simulations (cm)
0°	2.7	0°	2.76
119°	9.3	119°	9.27

Table 6.5: Comparison between the measured and simulation-determined parameters for the angular distribution measurement.

Nominal θ_{detector}	Target-detector distance (cm)	θ_{detector} inferred from simulations*	Target-detector distance from simulations (cm)
0°	18.2	2°	18.66
-25°	18.0	-21°	18.46
-55°	17.8	-51°	17.78
-73°	17.5	-68.3°	17.28
90°	17.5	90°	16.73

* We make reference to these angles in the subsequent tables. We also note that the efficiencies did not change significantly with small variations in θ_{detector}.

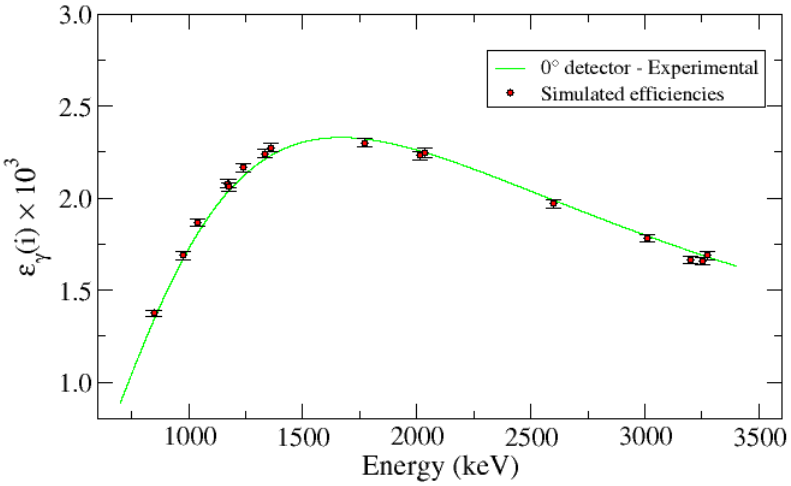

Figure 6.11: Comparison of the experimental efficiency curve with the simulated efficiencies for the 0° detector in the close-packed configuration.

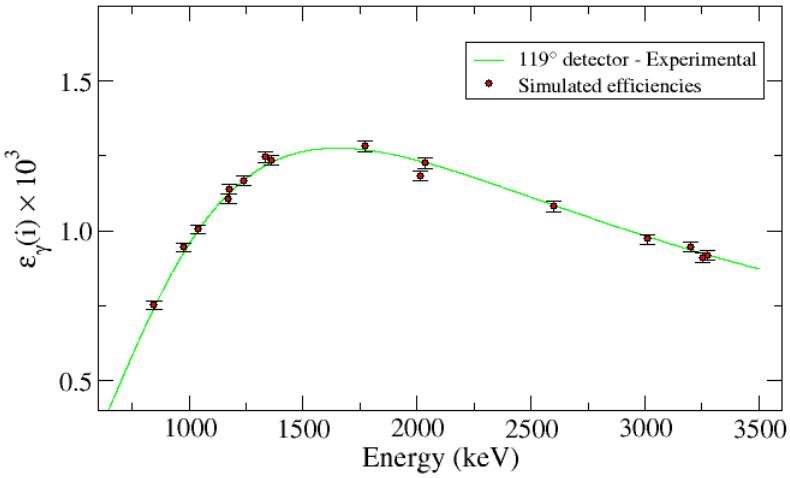

Figure 6.12: Comparison of the experimental efficiency curve with the simulated efficiencies for the 119° detector in the close-packed configuration.

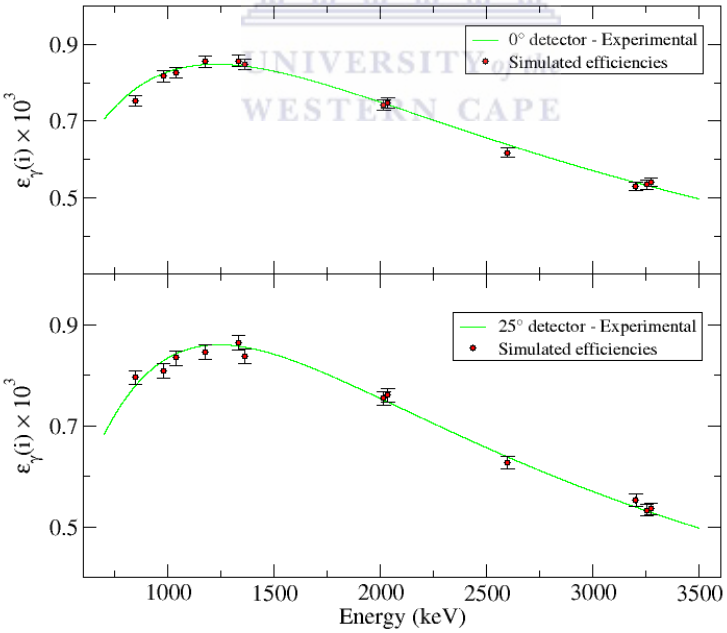

Figure 6.13: Comparison of the experimental efficiency curve with the simulated efficiencies for HPGe1 at 0° and 25° in the second configuration.

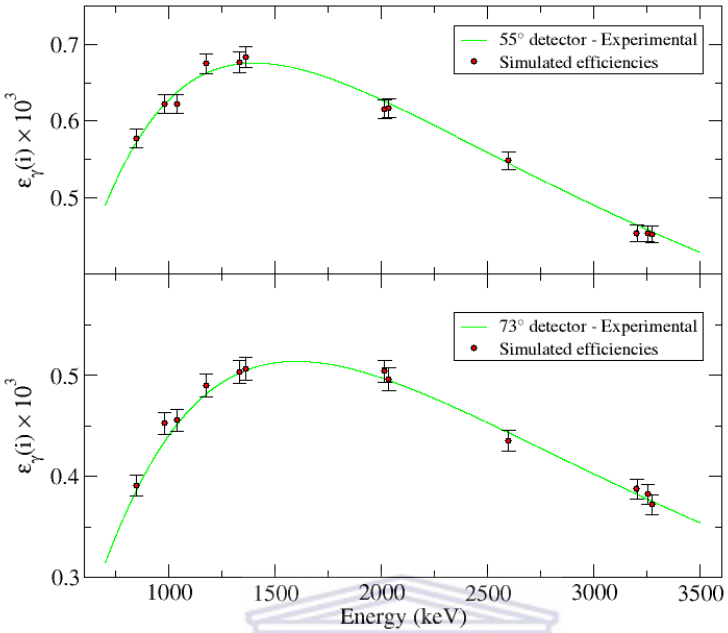

Figure 6.14: Comparison of the experimental efficiency curve with the simulated efficiencies for HPGe1 at 55° and 73° in the second configuration.

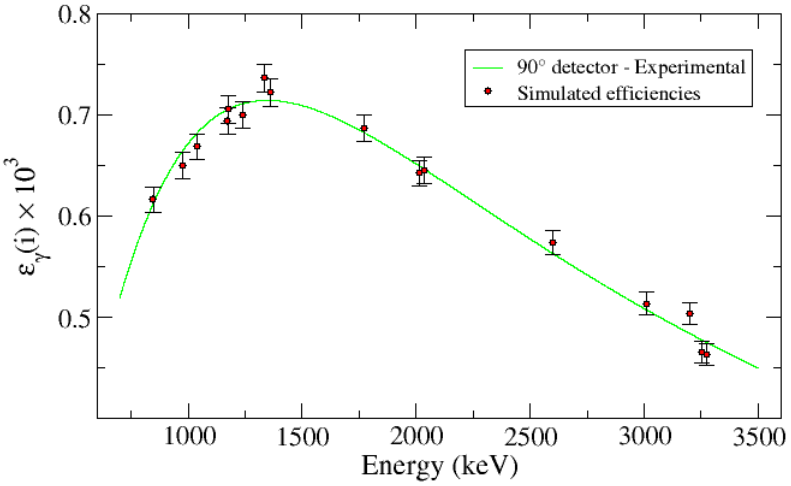

Figure 6.15: Comparison of the experimental efficiency curve with the simulated efficiencies for HPGe2 at 90° in the second configuration.

The results of our simulations showed that for many of the simulations, based on our χ^2 minimization test, the measured detector distances (angles) did not agree with the models (see Tables 6.4 and 6.5). For the remainder of the analysis we made the assumption that the detector angles and distances extracted from the simulations were a close approximation to the actual values. We then proceeded to run PENELOPE simulations for the ^{21}Ne(p,γ) gamma-rays. These are described below.

6.5 ^{21}Ne(p,γ) simulations

Since the photons from the ^{21}Ne(p,γ) experiment were emitted from a recoiling nucleus, the gamma energies in the laboratory frame would be Doppler-shifted depending on the angle subtended by the HPGe detector. In the non-relativistic limit, Doppler-shifted gamma-ray energy would be

$$E_\gamma = E_\gamma^0 \left(1 + \frac{v}{c}\cos\theta\right) \ , \tag{6.12}$$

where E_γ^0 is the unshifted γ-ray energy (for a source at rest), θ is the angle between the recoiling nucleus and the detector and v is the magnitude of the recoil velocity.

For this experiment, the γ-rays of interest had small Doppler shifts (of the order 0-4 keV, depending on the detector angle) due to the small recoil velocity of the ^{22}Na nucleus $\left(\frac{v}{c} \simeq 10^{-3}\right)$. Nonetheless, we used the Doppler shifted energies to run simulations and obtain the efficiencies of the detectors for the three gamma-rays of interest from ^{21}Ne$(p.\gamma)$, shown in Figure 4.3. The simulation procedure is described below.

6.5.1 Monte Carlo simulations for a distributed source of γ-rays from ^{21}Ne(p,γ).

The transformation method

One important aspect in Monte Carlo simulations is the use of random numbers. Random variables are generated statistically from a normalized uniform

probability density function (pdf) defined over some range. For example,

$$p(y)dy = \begin{cases} 1 & \text{for } 0 \leq y \leq 1, \\ 0 & \text{otherwise} \end{cases} \tag{6.13}$$

is a pdf that produces uniform random numbers (deviates) in the range $y \in [0, 1]$, such that

$$\int_{-\infty}^{\infty} p(y)dy = 1 \ . \tag{6.14}$$

For a given uniform random deviate x (defined in a certain range), if there exists a prescribed function $y(x)$, then the fundamental transformation law of probabilities demands that the probability distribution of x and y are the same [40],

$$|p(y)dy| = |p(x)dx| \tag{6.15}$$

or

$$p(y) = p(x)\left|\frac{dx}{dy}\right| \ . \tag{6.16}$$

Further, if one defines a cumulative density function (cdf)

$$x = F(y) = \int_{-\infty}^{y} p(y')dy' \ , \tag{6.17}$$

which ranges from 0 to 1, then it can easily be seen from Eqn. (6.16) that $p(x)$=1 is the pdf of x for $0 \leq x \leq 1$. By inspection of this result, together with the pdf defined in Eqn. (6.13), one can then easily generate random variables from a set of uniform deviates between 0 and 1 that follow a required probability distribution. More explicitly, for a given pdf $p(y)$ one can obtain for $0 \leq x \leq 1$ a set of random variables

$$y(x) = F^{-1}(x), \tag{6.18}$$

which follow the required pdf (if the inverse of the cdf exists). This approach is called the inverse transformation method to generate random variables for Monte Carlo simulations.

Randomizing the source position

In the simulations described till now the source of the calibration γ-rays was assumed to be a point, located at the center of the Tantalum foil shown in Fig. 6.10. However, since the ^{21}Ne target was made by implanting the ions over a circular spot of diameter 1.0 cm and the incident proton beam was rastered over a target diameter of 5 mm, the source of gammas from the $^{21}\mathrm{Ne}(p,\gamma)$ reaction was distributed over this circular region [2]. We modified the simulation program in PENELOPE to account for the extended distribution of the source by generating uniformly distributed positions for each emitted photon within a circle of radius 2.5 mm on the Ta backing. On using polar coordinates, one would think this requires the generation of a random 'radius' variable r between 0 and 2.5 mm and a random polar angle θ, between 0 and 2π. However, it is known that such an approach does not generate uniformly distributed random positions on the surface of a circle (see Fig. 6.16). This is understandable since the area element in polar coordinates is $dA = rdrd\theta$. Such an approach would lead to a clustering of points close to the origin as shown from the results of our simulations in Fig. 6.16. We therefore use the inverse transform method to generate these points of origin for the photons correctly. We define a probability density function $f(r)$ that ought to be proportional to r (given the area element mentioned above) with a normalization constant N

$$\int_0^R f(r)dr = 1 \qquad \Rightarrow \qquad \int_0^R N \cdot r dr = 1 \qquad \Rightarrow \qquad N = \frac{2}{R^2}$$

so that

$$f(r) = \frac{2}{R^2} r \ . \tag{6.19}$$

We then calculate the cumulative density function,

$$F(r) = \int_0^r f(r)dr \ = \ \frac{r^2}{R^2} \ . \tag{6.20}$$

By calculating the inverse of the cumulative density function one is able to get randomly distributed values of r on a circle of radius R

$$r = R\sqrt{U} \ , \tag{6.21}$$

[2] The effect of the implantation depth is assumed to be negligible for this analysis.

where U is a set of uniformly distributed random numbers between 0 and 1. Similarly, a random θ is generated between 0 and 2π

$$\theta = U \cdot 2\pi \ . \tag{6.22}$$

This method yields uniformly distributed points within a circle of radius R, which in our case is 2.5 mm.

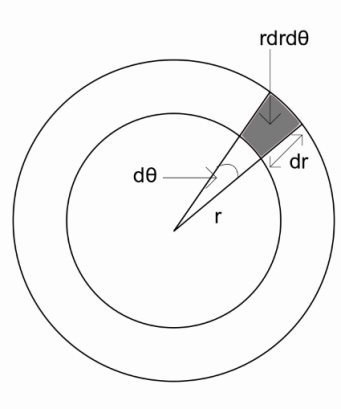

Figure 6.16: Area element in polar coordinates.

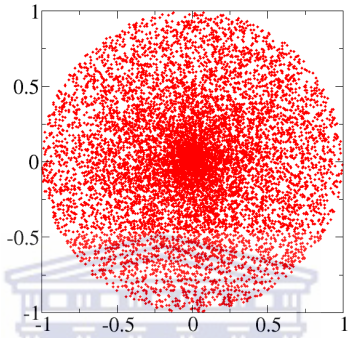

Figure 6.17: Clustering of points close to the origin obtained by the wrong simulation approach.

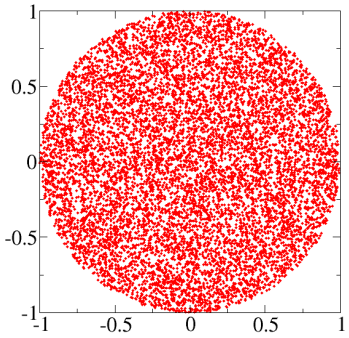

Figure 6.18: The correct distribution obtained correctly by the inverse transformation method.

The results of our simulations for $^{21}\mathrm{Ne}(p,\gamma)$ photons are shown in the Tables and figures below [3]. It is apparent that the water cooling significantly attenuates all three gamma-rays for detectors placed at 0° and 25°.

Table 6.6: Comparison of source calibration efficiencies with the simulated efficiencies.

$E_\gamma = 1295$ keV		
Detector angle	$\epsilon_\gamma \times 10^3$ from source calibration	$\epsilon_\gamma \times 10^3$ from simulation
0°	2.187(223)	2.047(26)
119°	1.178(39)	1.179(17)

[3] We ran 4×10^6 primary showers for the close-packed configuration and 16×10^6 showers for the angular-distribution configuration.

Table 6.7: Comparison of source calibration efficiencies with the simulated efficiencies.

$E_\gamma = 1369$ keV		
Detector angle	$\epsilon_\gamma \times 10^3$ from source calibration	$\epsilon_\gamma \times 10^3$ from simulation
0°	2.254(136)	2.098(23)
119°	1.206(32)	1.238(18)

Table 6.8: Comparison of source calibration efficiencies with the simulated efficiencies.

$E_\gamma = 1952$ keV		
Detector angle	$\epsilon_\gamma \times 10^3$ from source calibration	$\epsilon_\gamma \times 10^3$ from simulation
0°	2.283(502)	2.075.(23)
119°	1.236(71)	1.256(18)

Table 6.9: Comparison of source calibration efficiencies with the simulated efficiencies.

$E_\gamma = 1295$ keV		
Detector angle	$\epsilon_\gamma \times 10^3$ from source calibration	$\epsilon_\gamma \times 10^3$ from simulation
0°	0.856(20)	0.802(7)
−21°	0.861(19)	0.799(7)
−51°	0.673(11)	0.686(6)
−68.3°	0.503(8)	0.503(5)
90°	0.714(21)	0.708(6)

Table 6.10: Comparison of source calibration efficiencies with the simulated efficiencies.

$E_\gamma = 1369$ keV		
Detector angle	$\epsilon_\gamma \times 10^3$ from source calibration	$\epsilon_\gamma \times 10^3$ from simulation
0°	0.853(12)	0.798(7)
−21°	0.857(11)	0.791(7)
−51°	0.676(7)	0.689(6)
−68.3°	0.506(6)	0.508(5)
90°	0.714(12)	0.713(6)

Table 6.11: Comparison of source calibration efficiencies with the simulated efficiencies.

$E_\gamma = 1952$ keV		
Detector angle	$\epsilon_\gamma \times 10^3$ from source calibration	$\epsilon_\gamma \times 10^3$ from simulation
$0°$	0.761(39)	0.715(6)
$-21°$	0.763(36)	0.725(6)
$-51°$	0.630(22)	0.628(6)
$-68.3°$	0.500(19)	0.496(5)
$90°$	0.658(41)	0.649(6)

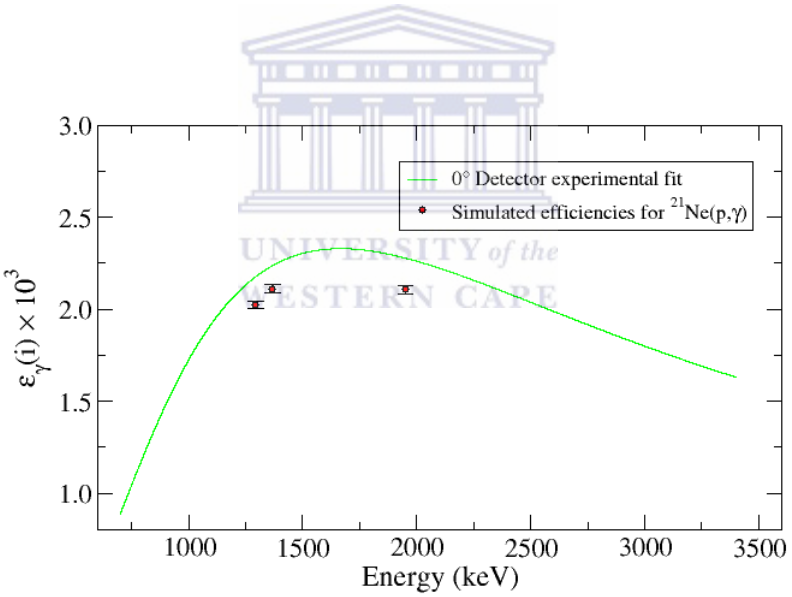

Figure 6.19: Comparison of experimental efficiency curve with results from the simulation of $^{21}\mathrm{Ne}(p,\gamma)$ gamma rays for HPGe1 in close-packed configuration.

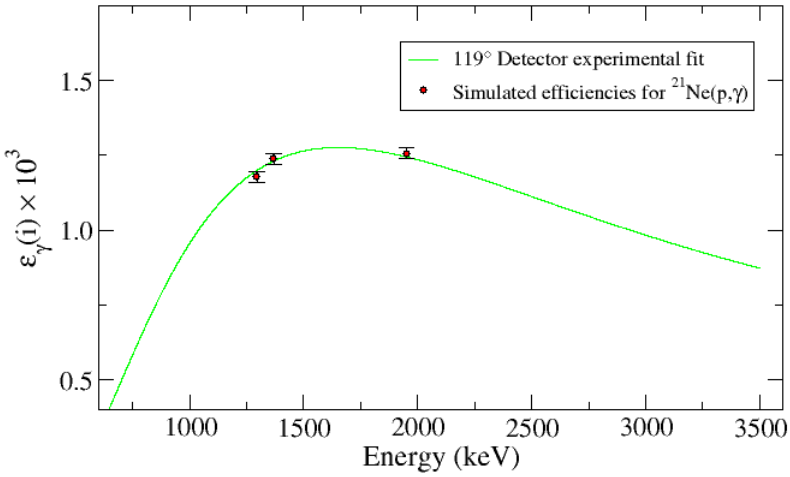

Figure 6.20: Comparison of experimental efficiency curve with results from the simulation of $^{21}\mathrm{Ne}(p,\gamma)$ gamma rays for HPGe2 in close-packed configuration.

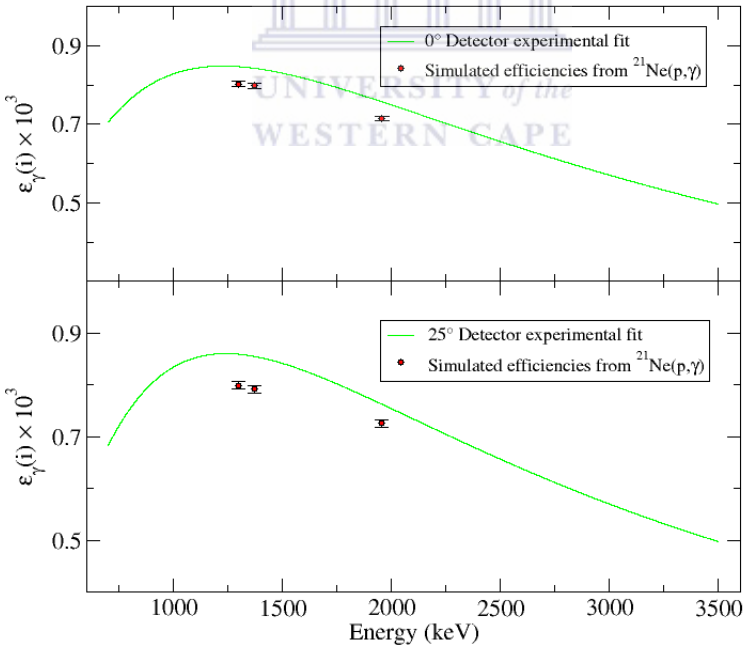

Figure 6.21: Comparison of experimental efficiency curve with results from the simulation of $^{21}\mathrm{Ne}(p,\gamma)$ gamma rays for HPGe1 in the 'angular distribution' configuration.

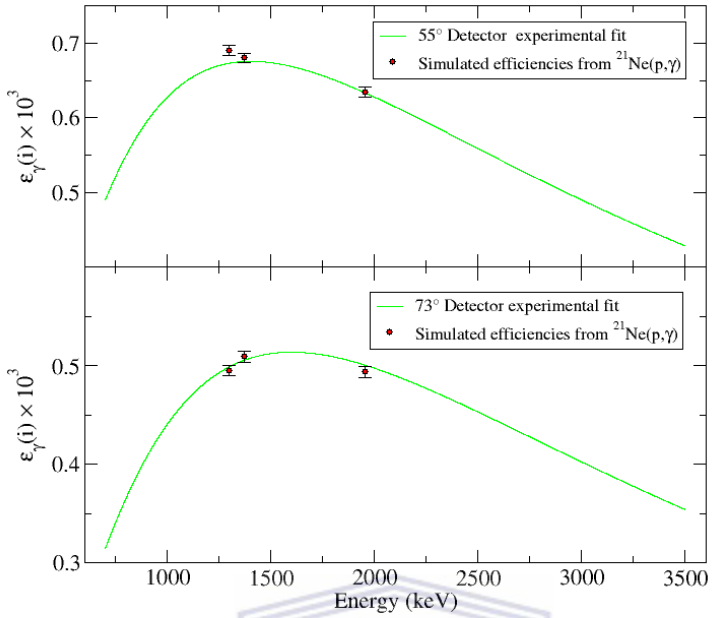

Figure 6.22: Comparison of experimental efficiency curve with results from the simulation of $^{21}\mathrm{Ne}(p,\gamma)$ gamma rays for HPGe2 in the 'angular distribution' configuration.

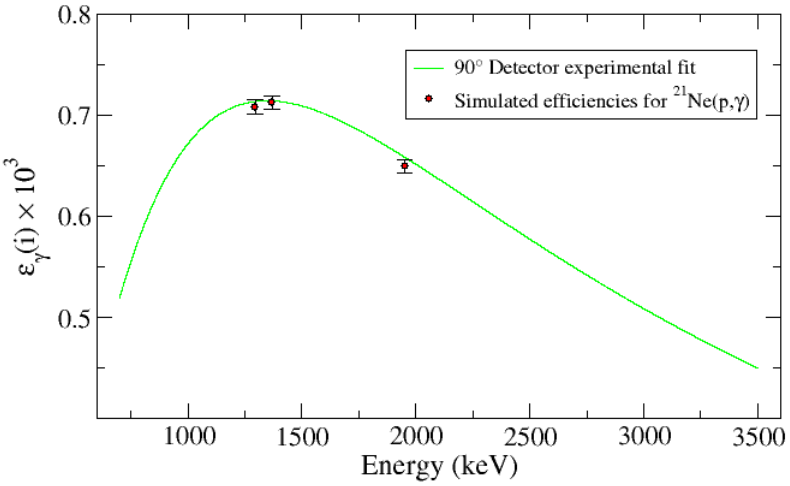

Figure 6.23: Comparison of experimental efficiency curve with results from the simulation of $^{21}\mathrm{Ne}(p,\gamma)$ gamma rays for HPGe2 in the 'angular distribution' configuration.

Simulations to check dependence on multipolarity

Referring to Fig. 4.3, the 1952 $\rightarrow$ 657 keV transition is of pure $E2$ isoscalar nature emitting a 1295 keV gamma-ray. On the other hand, the other two gammas of interest from the 1952 $\rightarrow$ 583 keV (E_γ = 1369 keV) and the 1952 $\rightarrow$ 0 keV transitions (E_γ = 1952 keV) are mixed isovector transitions with potentially strong $M1$ character. Purely on the basis of the isospin selection rules described in Section 3.4, one can assume that the $E2$ matrix elements in the latter transitions are strongly suppressed. An angular correlation measurement performed during the late 1960's supports this assumption for the 1952 $\rightarrow$ 583 keV transition where the authors measured the $E2/M1$ mixing ratio to be (0.04$\pm$0.06) [45]. We defer a discussion on this measurement to the next chapter. The close-packed configuration should in principle wash out all multipolarity dependent angular distribution effects for a branching ratio measurement. We performed further Monte Carlo simulations to check if this is the case. The angular distribution of the gamma-rays with respect to the beam axis should have a form

$$W_d(\theta) = 1 + P_2(\cos\theta) \ , \tag{6.23}$$

for a pure dipole, and

$$W_q(\theta) = 1 + P_2(\cos\theta) + P_4(\cos\theta) \ , \tag{6.24}$$

for a quadrupole transition.

For our PENELOPE simulations we generated gamma-rays with both these distributions for the three gamma-rays of interest, with the detectors in the close-packed configuration. This was performed using the Von Neumann's acceptance-rejection method described below. The locations of the gammas from the target were randomly generated as mentioned previously.

The acceptance - rejection method

The acceptance-rejection method is another technique to generate random variables whose pdf is known. But this method can be computationally expensive and is based on the fact that the area under a pdf $p(x)$ corresponds

to the probability of generating a random number x in that range. In particular, one can save computational time by using a comparison function $f(x)$ which has a finite area and lies above the curve $p(x)$. One can then randomly choose a point in two dimensions that is uniformly distributed in the area under $f(x)$. Whenever this randomly selected point lies inside the area under the original pdf $p(x)$ it is accepted and when it lies outside it is rejected. This is called the acceptance-rejection method [40] and is geometrically shown in Fig. 6.24

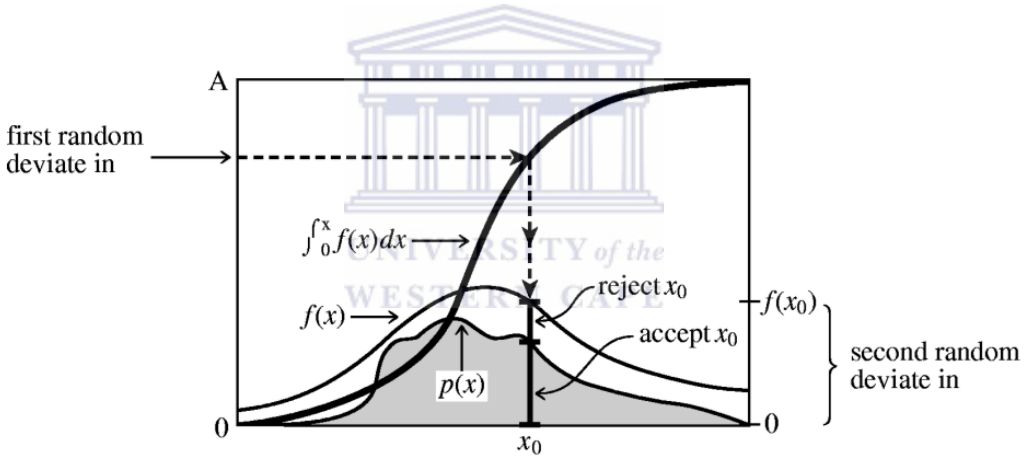

Figure 6.24: Rejection method for generating a random number x_0 that is only accepted if it falls under the probability distribution $p(x)$ curve and rejected otherwise. Figure taken from [40].

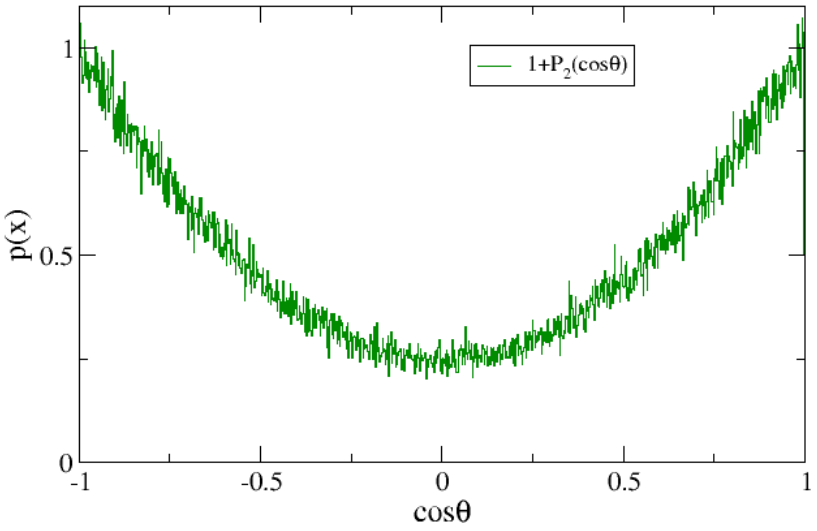

Figure 6.25: Histogrammed normalized pdf of $W_d(\theta)$ generated for 10^6 events using the acceptance-rejection method.

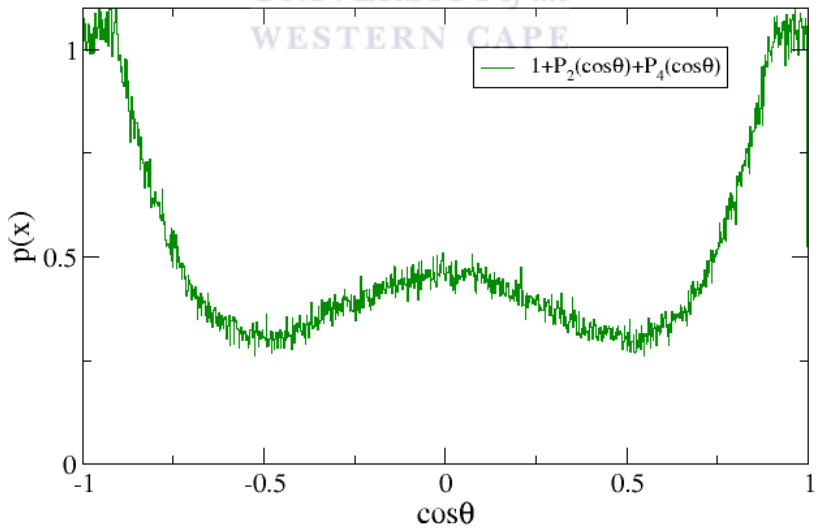

Figure 6.26: Histogrammed normalized pdf of $W_q(\theta)$ generated for 10^6 events using the acceptance-rejection method.

In order to generate gamma-rays that followed a specific angular distribution we added a subroutine to the PENELOPE code to generate the photon directions according to the pdfs shown in Figs. 6.25 and 6.26. Our simulations show that roughly 50% of the events were rejected for these pdfs thereby doubling our simulation time. The results of our simulations shown in Tables 6.12 and 6.13 show that the angular distributions did not have significant effect for the efficiencies of the detectors in the close-packed configuration.

Table 6.12: HPGe1

E_γ keV	$\epsilon_\gamma \times 10^3$ (isotropic)	$\epsilon_\gamma \times 10^3$ (dipole)	$\epsilon_\gamma \times 10^3$ (quadrupole)
1295	2.047(26)	2.073(23)	2.061(23)
1369	2.098(23)	2.077(23)	2.053(23)
1952	2.075(23)	2.148(23)	2.083(23)

Table 6.13: HPGe2

E_γ keV	$\epsilon_\gamma \times 10^3$ (isotropic)	$\epsilon_\gamma \times 10^3$ (dipole)	$\epsilon_\gamma \times 10^3$ (quadrupole)
1295	1.179(17)	1.197(12)	1.221(18)
1369	1.238(18)	1.272(18)	1.198(18)
1952	1.256(18)	1.229(18)	1.214(18)

6.6 Sorting and analysis of ^{21}Ne(p,γ) data

The ^{21}Ne(p,γ) data were sorted using the JAM program to generate histograms of various spectra. A sample γ-ray singles spectrum from HPGe1 in the close-packed configuration is shown below. We clearly identify the peaks of interest from transitions in ^{22}Na following the deexcitation of the 1952 keV level. We also identify 10 other γ rays from the resonance that arise from feeding to higher lying states in ^{22}Na (see Fig. 6.28). We discuss some aspects of this spectrum below.

In addition to the gammas generated from the ^{21}Ne(p,γ) resonance (Table 6.14) we also identify several contaminant peaks in the spectrum shown in Fig. 6.27 and Table 6.15.

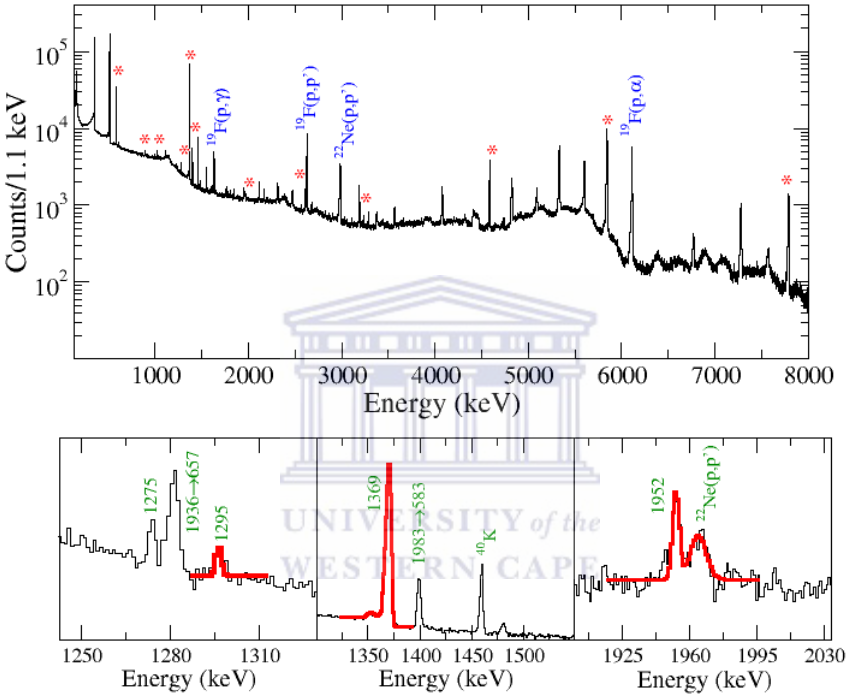

Figure 6.27: Top panel: Singles γ-ray spectrum from HPGe1 in close-packed configuration. Contaminant peaks are clearly labeled. Bottom panel: The three gamma-rays of interest from the 1952 keV state shown with their fits. The broad 1966 keV line is an escape peak of the 2988 keV gamma ray shown in Table 6.15.

Table 6.14: Gamma rays from the $^{21}\mathrm{Ne}(p,\gamma)$ resonance.

E_γ (keV)	Transition $E_i \rightarrow E_f$ (keV)
583	$583 \rightarrow 0$
891	$891 \rightarrow 0$
1093	$1983 \rightarrow 891$
1295	$1952 \rightarrow 657$
1369	$1952 \rightarrow 583$
1400	$1983 \rightarrow 583$
1952	$1952 \rightarrow 0$
1983	$1983 \rightarrow 0$
2626	$7800 \rightarrow 5174$
3191	$5174 \rightarrow 1983$
4591	$5174 \rightarrow 583$
5848	$7800 \rightarrow 1952$
7800	$7800 \rightarrow 0$

Table 6.15: Beam induced contaminants.

E_γ (keV)	Source of beam related contaminant
1275	^{22}Na β decay + $^{22}\mathrm{Ne}(p,p')$
1281	From non-resonant capture*
1634	$^{19}\mathrm{F}(p,\gamma)$
1968	$^{22}\mathrm{Ne}(p,p')$
2780	$^{19}\mathrm{F}(p,p')$
2988	$^{22}\mathrm{Ne}(p,p')$
6129	$^{19}\mathrm{F}(p,\alpha)$

*This effect proceeds via a $1936 \rightarrow 657$ keV transition in ^{22}Na.

The main contaminant peaks (ignoring room background) arise from ^{19}F and ^{22}Ne impurities in the target. The ^{19}F contamination is a common effect observed while using Tantalum backings [46] and can easily be identified from a 6129 keV peak arising from strong $^{19}\mathrm{F}(p,\alpha\gamma)$ resonances. The ^{22}Ne contamination in the target can be explained by tails in the momentum distribution of the mass-separated ions during the implantation process. It is possible that the momentum profile was highly asymmetrical as we find no indication of ^{20}Ne implantation from our spectra.

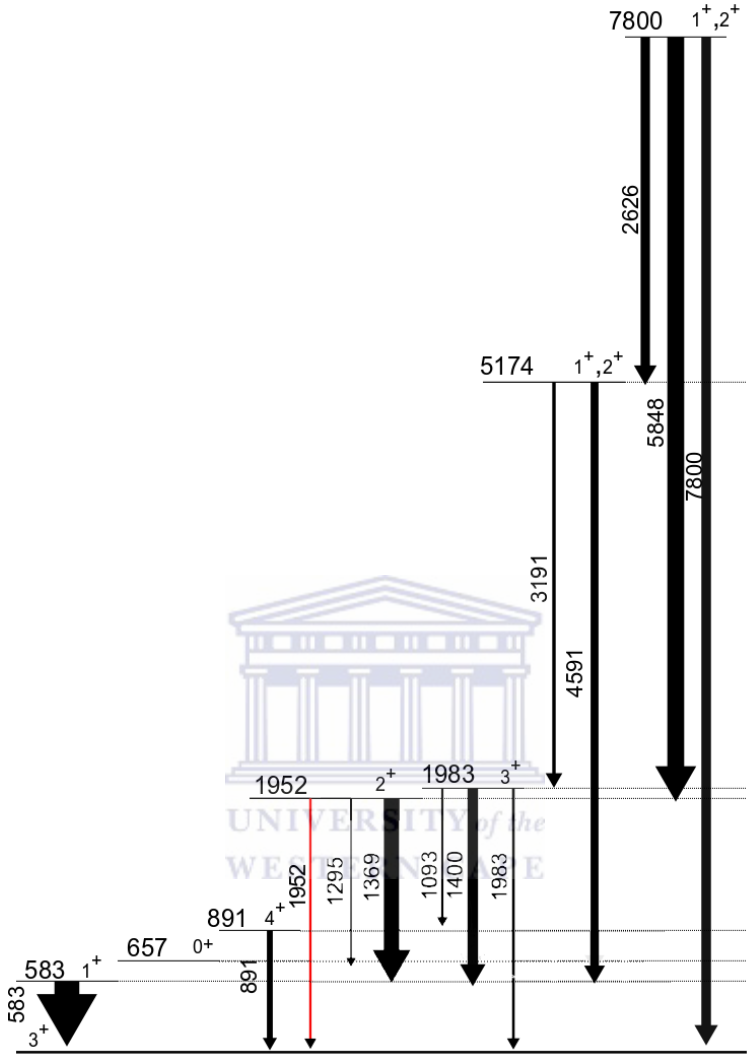

Figure 6.28: Transitions from the 7800 keV level that are observed in our experiment.

The coincidence spectra shown in the figures below offer a diagnostic tool to verify our peak identification for analysis. These spectra were not used for the final branching fraction determination due to lack of statistics. Fig. 6.29 shows the singles γ-ray spectrum from the NaI detector in the close-packed configuration. The coincident HPGe spectra were obtained by gating on the $E_\gamma = 5848$ keV peak in the NaI detector and the prompt TAC peaks for HPGe1 and HPGe2 respectively (see Figs. 6.29 and 6.30).

As shown in Fig. 6.31, the coincidences show that the 1952 keV peak indeed arises from the $E_x = 7800 \rightarrow 1952 \rightarrow 0$ keV transitions. Due to the limitations of the low resolution NaI detector, Figs. 6.32-6.35 were further used as diagnostic tools to check the reliability of our energy gates to generate the coincidences.

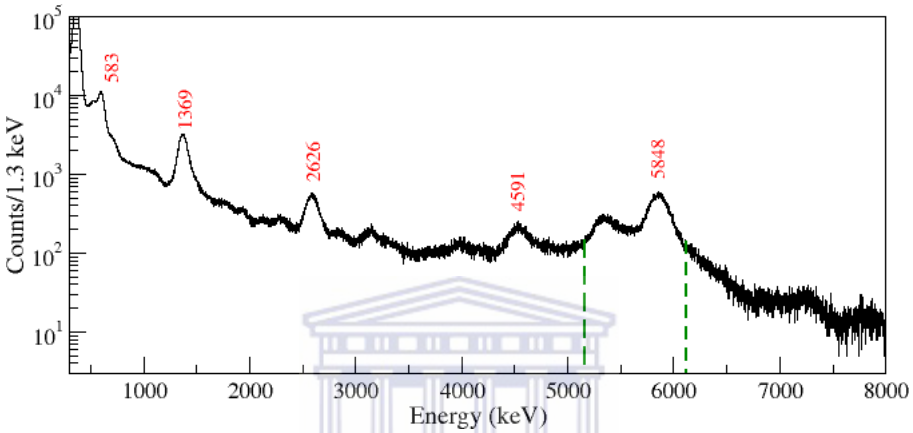

Figure 6.29: Singles γ-ray spectrum from the NaI detector. The NaI energy gate used to generate coincidences is shown.

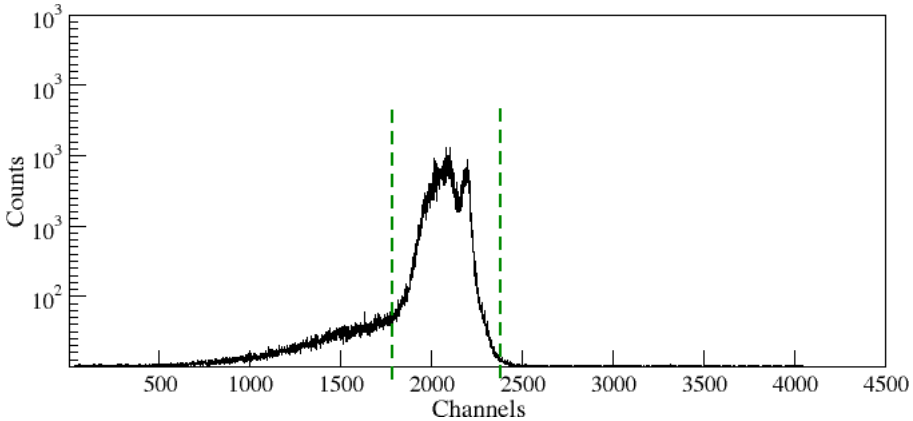

Figure 6.30: A sample TAC spectrum with the gated region that was used to generate the coincidence spectrum shown below.

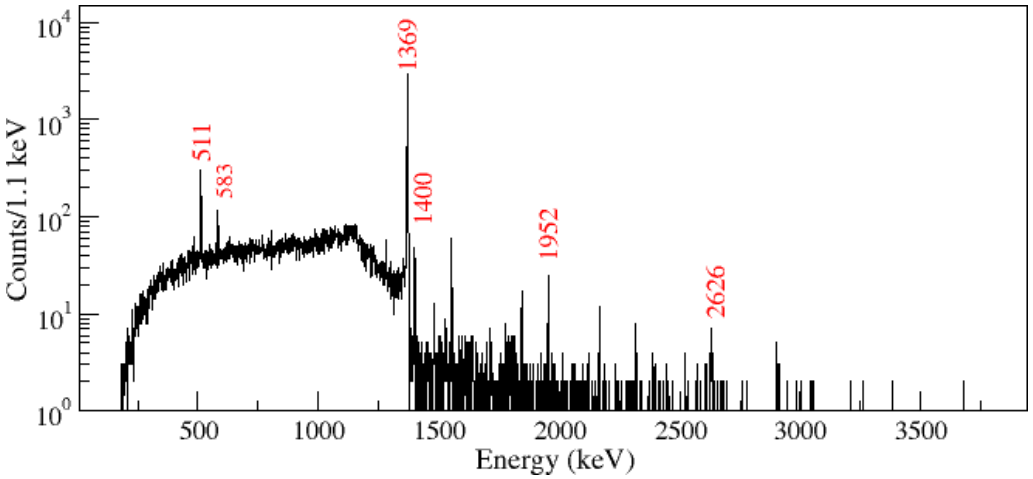

Figure 6.31: HPGe1 coincidence spectrum generated with the gate shown above. The prominent gamma lines from ^{22}Na are labeled.

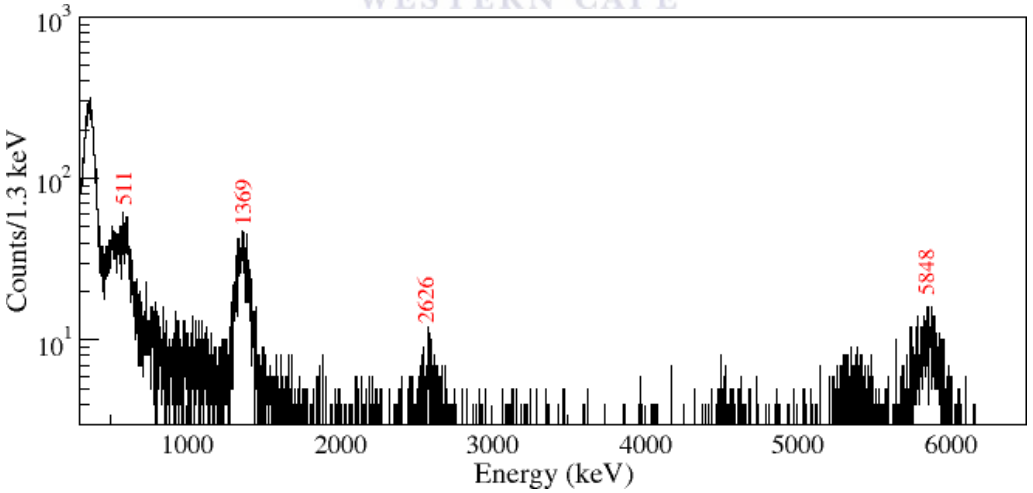

Figure 6.32: NaI coincidence spectrum generated by gating on 583 keV gamma peak of HPGe1.

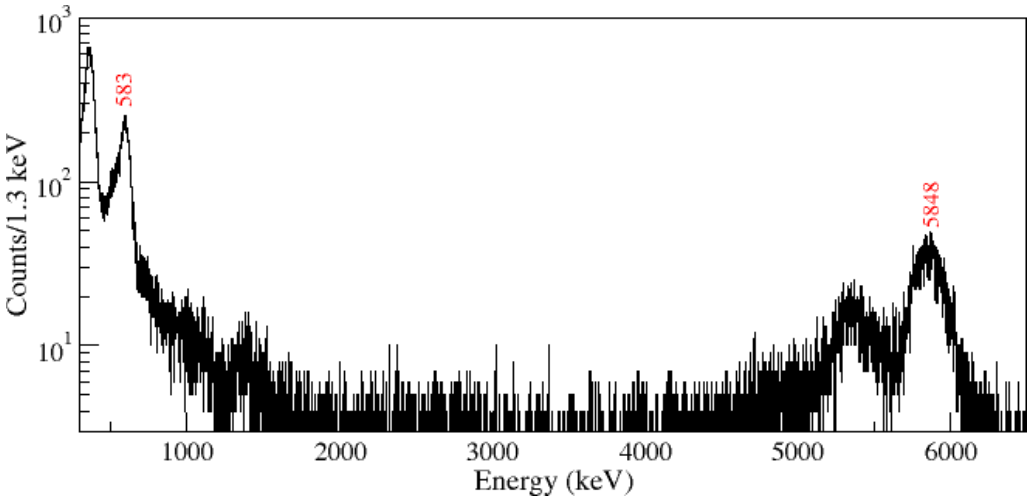

Figure 6.33: NaI coincidence spectrum generated by gating on 1369 keV gamma peak of HPGe1. .

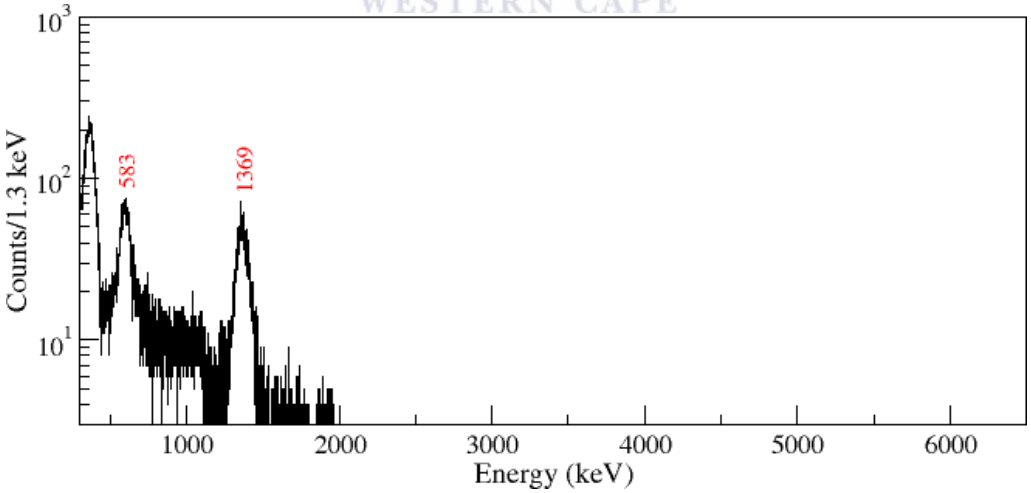

Figure 6.34: NaI coincidence spectrum generated by gating on 5848 keV gamma peak of HPGe1.

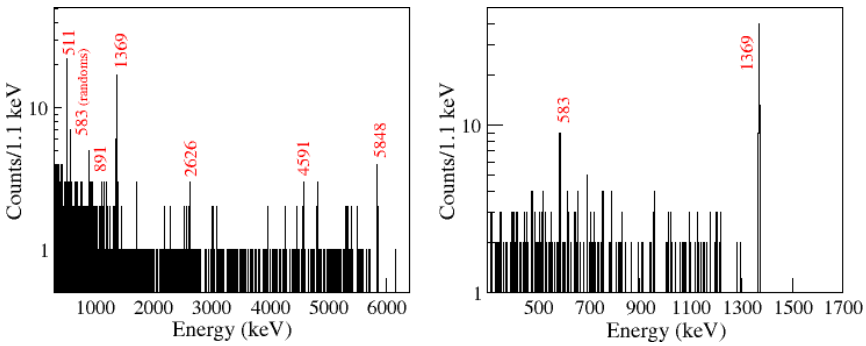

Figure 6.35: HPGe2 in coincidence with HPGe1 gated on 583 keV (left) and 5848 (right) keV.

6.7 Branching ratio determination

The photo peak areas of the three gamma-rays of interest $N_\gamma(i)$ from the close-packed configuration were used to calculate the branching ratio $Br(i)$ using the formula

$$Br(i) = \frac{N_\gamma(i)}{\sum_{j=1}^{3} N_\gamma(j) \cdot \frac{\epsilon_\gamma(i)}{\epsilon_\gamma(j)}} , \tag{6.25}$$

where $\epsilon_\gamma(i)$ and $\epsilon_\gamma(j)$ were obtained from the simulations. The results from both detectors are shown in the tables below.

Table 6.16: Relative branches from HPGe1.

Energy (keV)	$Br(i)$ (%)
1295	0.236(41)
1369	98.983(57)
1952	0.781(41)

Table 6.17: Relative branches from HPGe2.

Energy (keV)	$Br(i)$ (%)
1295	0.257(57)
1369	98.756(95)
1952	0.987(77)

6.8 Angular distribution data

In the second configuration we obtained angular distribution information for the 1369 and 1952 keV gamma rays. Fig. 6.36 show angular distribution for the 1952 keV gamma-ray. Clearly the data lack statistics to infer the multipolarity of the transition. The isospin selection rules discussed in Section. 4.4 suggest the $E2$ matrix element for this $2^+ \rightarrow 3^+$ $\Delta T = 1$ transition to be small relative to the $M1$ matrix element. However, this need not be true in general as isospin is not a good quantum number in describing nuclei.

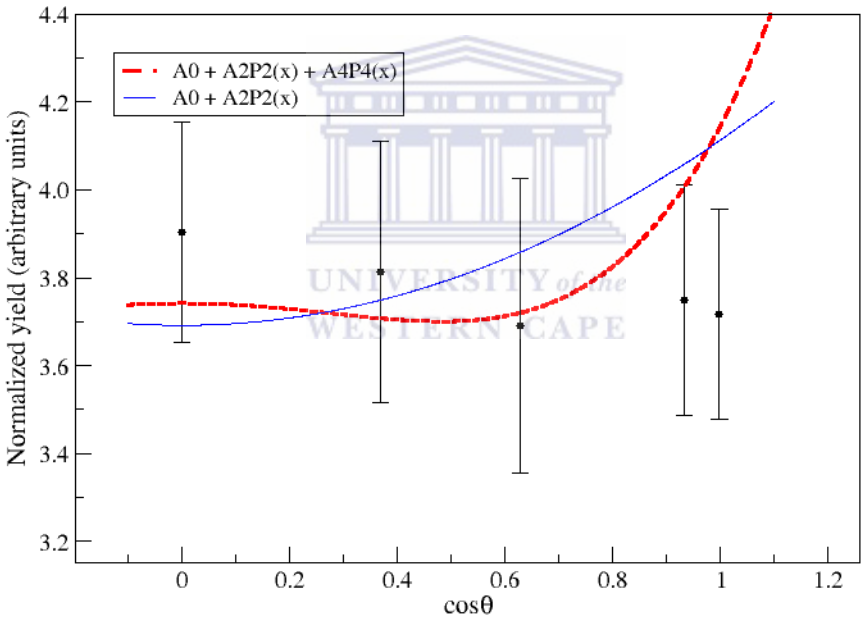

Figure 6.36: Angular distribution of the 1952→0 keV transition. The yield is normalized to the summed area of all the peaks listed in Table. 6.14 from HPGe2, postioned at 90° to the beam.

On extracting the angular distribution of the 1369 keV gamma-ray which arises from a $2^+ \rightarrow 1^+$ $\Delta T = 1$ transition, it is clear (see Fig. 6.37) that

a significant quadrupole component is required to describe the data, particularly at 55°, where $P_2(\cos\theta)$ vanishes. This is in contradiction with the isospin selection rule favoring strong isovector $M1$ transitions relative to $E2$ transitions. Our result is also in conflict with an older measurement of the mixing ratio [45] which suggests that the $E2$ component should be negligible. The latter should not be surprising as angular correlation measurements in those days were performed with poor resolution NaI scintillator detectors. Nonetheless, clearly more data are required to obtain the $E2/M1$ mixing ratio for the 1952→0 keV transition of interest which is relavant for this work.

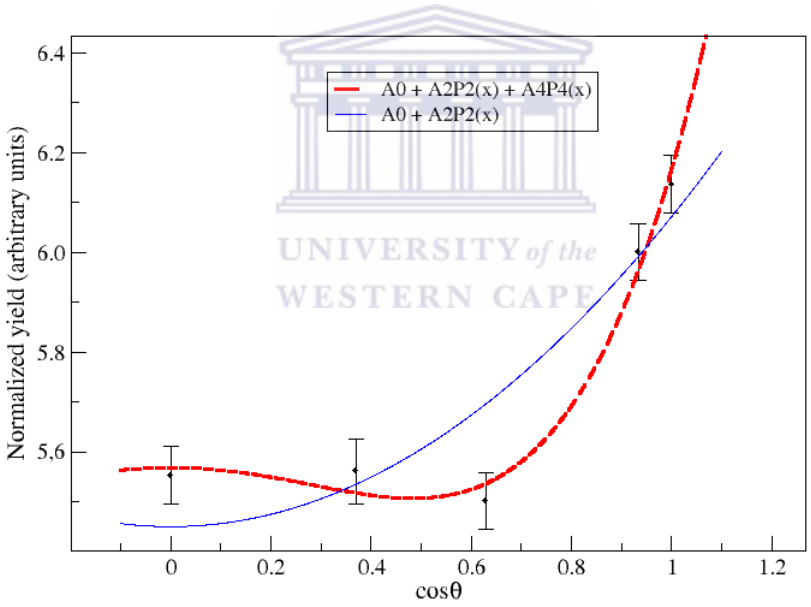

Figure 6.37: Angular distribution of the 1952→583 keV transition. The yield is normalized to the summed area of all the peaks listed in Table. 6.14 from HPGe2, postioned at 90° to the beam.

Chapter 7

Conclusions and future directions

Assuming that the 1952 $\rightarrow$ 0 keV transition is purely $M1$, we can extract the partial width of the $2_1^+ \rightarrow 3^+$ decay in ^{22}Na from the total width $\Gamma = 0.057 \pm 0.0143$ eV [33], using

$$\Gamma_{M1} = \Gamma \cdot Br(1952 \rightarrow 0) \, . \tag{7.1}$$

The weak magnetism form factor can then easily be calculated using Eq. (4.10). Finally, we use the A_{22} $\beta - \gamma$ correlation coefficient from the Berkeley measurement and Eq. 4.14, to obtain both B and the tensor form factor D shown in Table. 7.1.

Table 7.1: Partial width and the form factors obtained from the HPGe1 and HPGe2.

Detector	Γ_{M1} $\times 10^{-4}$ eV	b	B †	D
HPGe1	4.5(1.1)	4.5(6)	-13.5(1.7)	25.6(5.9)
HPGe2	5.6(1.5)	5.1(7)	-15.2(2.0)	27.2(6.0)

†B and c_1 should have opposite sign to prevent c_2 from attaining unrealistically large values [2, 32].

In order to calculate the D term, the axial-vector form factor $c_1 = 0.015$ [1] was obtained from the ratio of the ft value of pure Fermi superallowed de-

[1]The uncertainty in c_1 is small and neglected.

cays to that of ^{22}Na decay[2] so that $c_1 = \sqrt{2ft^{fermi}/ft(^{22}\mathrm{Na})}$ [48], with $ft^{fermi} = 3072.27 \pm 0.72$ s [47]. The second-order axial-vector form factor was set to $c_2 \approx 0$ following the arguments of Ref. [32].

It is clear from Table 7.1 that although we make an unambiguous first measurement of the $2_1^+ \rightarrow 3^+$ branch in ^{22}Na, our results, which are higher than the quoted unpublished value of Ref [2] do not resolve the issue regarding the anomalously large G-parity violating induced-tensor form factor from ^{22}Na beta decay. The ratios of the $E2$ to $M1$ transition strengths in terms of the Weisskopf single particle estimates described in Section 3.3 are 2.8×10^{-4} for the 1369 keV gamma-ray and 5.4×10^{-4} for the 1952 keV gamma-ray. A shell model calculation on the other hand, using the NuShellX code with the USD-B interaction shows that the $M1$ strength relative to the $E2$ is smaller by a factor of 2 for the 1952→0 keV transition, while it is 75 times stronger for the more intense 1952→583 keV transition [49]. Clearly a measurement of the $E2/M1$ mixing for the 1952→0 keV transition will offer a path ahead. But measuring the mixing ratio for such a weak branch will be challenging.

It is interesting that our angular distribution data indicate a strong $E2$ component to the matrix element for the 1952→583 keV isovector transition . Since the ^{22}Na nucleus is known to be highly deformed, with well known rotational bands [50], it is possible that K-quantum number selection rules suppress the dipole component relative to the quadrupole for both cases, based on K-forbiddenness. The role of isospin mixing also needs to be investigated in some more detail to better explain our results.

[2]Isospin-symmetry breaking corrections in ^{22}Na beta decay were neglected as they are assumed to be small compared to our uncertainties.

Appendix A

Least Squares Fitting

Suppose one wants to fit a line to a set of data, say $(x_i,\ y_i)$. A very useful function used for such fitting is a power-series polynomial of the form

$$y(x) = a_1 + a_2 x + a_3 x^2 + a_4 x^3 + \cdots + a_m x^{m-1} \ , \tag{A.1}$$

where the dependent variable y is expressed as a sum of power series of the independent variable x with coefficients $a_1,\ a_2,\ a_3,\ a_4$, and so forth. To do so one have to first find the values of the a_k's coefficients that minimize the discrepancy between the variable y and the independent variable x. Lets rewrite Eqn. (A.1) as

$$y(x) = \sum_{k=1}^{m} a_k x^{k-1} = \sum_{k=1}^{m} a_k f_k(x). \tag{A.2}$$

For any estimated values of the coefficients a_k's, one can calculate the probability of obtaining the measurement y_i with standard deviation σ_i as

$$P(a_k) = \prod \left(\frac{1}{\sigma_i \sqrt{2\pi}} \right) \exp \left\{ -\frac{1}{2} \sum \frac{1}{\sigma_i^2} \left[y_i - \sum_{k=1}^{m} a_k f_k(x_i) \right]^2 \right\}. \tag{A.3}$$

Because the first factor in the product of Eqn. (A.3) is not dependent on the values of the coefficients, maximizing the probability $P(a_k)$ is equivalent to minimizing the sum in the exponential. The sum is defined to be the goodness-of-fit coefficient χ^2

$$\chi^2 = \sum \left[\frac{1}{\sigma_i} \left[y_i - \sum_{k=1}^{m} a_k f_k(x_i) \right] \right]^2 \tag{A.4}$$

To find the values of the coefficients that yields the minimum value of χ^2, the partial derivative of the χ^2 with respect to the coefficients is set to zero

$$\begin{aligned}\frac{\partial}{\partial a_l}\chi^2 &= \frac{\partial}{\partial a_l}\sum\left[\frac{1}{\sigma_i}\left[y_i - \sum_{k=1}^{m} a_k f_k(x_i)\right]\right]^2 \\ &= -2\sum\left\{\frac{f_l(x_i)}{\sigma_i^2}\left[y_i - \sum_{k=1}^{m} a_k f_k(x_i)\right]\right\} \\ &= 0\end{aligned} \tag{A.5}$$

From Eqn. (A.5) one can obtain a set of m coupled linear equations for the m coefficients a_l, with the index l running from 1 to m:

$$\sum y_i \frac{f_l(x_i)}{\sigma_i^2} = \sum_{k=1}^{m}\left\{a_k \sum\left[\frac{1}{\sigma_i^2} f_l(x_i) f_k(x_i)\right]\right\} \ . \tag{A.6}$$

The solutions to Eqn. (A.6) are found by the method of determinants. Eqn. (A.7) display the solution to the a_1 coefficient,

$$a_1 = \frac{1}{\Delta}\begin{bmatrix} \sum y_i \frac{f_l(x_i)}{\sigma_i^2} & \sum \frac{f_1(x_i)f_2(x_i)}{\sigma_i^2} & \sum \frac{f_1(x_i)f_3(x_i)}{\sigma_i^2} & \cdots \\ \sum y_i \frac{f_2(x_i)}{\sigma_i^2} & \sum \frac{f_2(x_i)f_2(x_i)}{\sigma_i^2} & \sum \frac{f_2(x_i)f_3(x_i)}{\sigma_i^2} & \cdots \\ \sum y_i \frac{f_3(x_i)}{\sigma_i^2} & \sum \frac{f_3(x_i)f_2(x_i)}{\sigma_i^2} & \sum \frac{f_3(x_i)f_3(x_i)}{\sigma_i^2} & \cdots \\ \vdots & \vdots & \vdots & \vdots \end{bmatrix} \ , \tag{A.7}$$

with

$$\Delta = \begin{bmatrix} \sum \frac{f_1(x_i)f_1(x_i)}{\sigma_i^2} & \sum \frac{f_1(x_i)f_2(x_i)}{\sigma_i^2} & \sum \frac{f_1(x_i)f_3(x_i)}{\sigma_i^2} & \cdots \\ \sum \frac{f_2(x_i)f_1(x_i)}{\sigma_i^2} & \sum \frac{f_2(x_i)f_2(x_i)}{\sigma_i^2} & \sum \frac{f_2(x_i)f_3(x_i)}{\sigma_i^2} & \cdots \\ \sum \frac{f_3(x_i)f_1(x_i)}{\sigma_i^2} & \sum \frac{f_3(x_i)f_2(x_i)}{\sigma_i^2} & \sum \frac{f_3(x_i)f_3(x_i)}{\sigma_i^2} & \cdots \\ \vdots & \vdots & \vdots & \vdots \end{bmatrix} \tag{A.8}$$

Appendix B

Gauss-Jordan Elimination

The method of least squares requires a solution of a set of n simultaneous equations in n unknowns a_i similar to the following matrix

$$[y_k] = [a_j][X_{kj}] \ . \tag{B.1}$$

One could multiply the matrix in Eqn. (B.1) by another matrix X^{-1}, the inverse matrix. This multiplication gives the solutions to the coefficients a_j

$$[y_k][X_{kj}]^{-1} = [a_j]1 = [a_j] \ . \tag{B.2}$$

The expression in Eqn. (B.2) can be rewritten more conveniently to give the solution for each of the coefficients a_j in the form

$$a_j = \sum_{k=1}^{n} (y_k X_{kj}^{-1}) \ . \tag{B.3}$$

Thus, the solutions to the coefficients a_j in Eqn. (B.1) has been reduced to evaluating the inverse matrix X^{-1}.

To evaluate the matrix X^{-1}, one can use the Gauss-Jordan Elimination method to invert a matrix X from a unity matrix while reducing the original matrix to unity. Consider the inverse matrix X^{-1} as the ratio of the unity matrix divided by the original matrix, $X^{-1} = 1/X$. If the numerator and denominator are manipulated in the same manner (multiplying rows or columns by the same constant factor and adding the same rows scaled to the

same constants), the ratio remains unchanged. If the manipulation are done properly, one can change the denominator into the unity matrix; then the numerator becomes equal to the inverse matrix X^{-1}. Consider a 3×3 matrix A and 3×3 unity matrix.

$$\begin{bmatrix} X_{11} & X_{12} & X_{13} \\ X_{21} & X_{22} & X_{23} \\ X_{31} & X_{32} & X_{33} \end{bmatrix} \qquad \begin{bmatrix} 1 & 0 & 0 \\ 0 & 1 & 0 \\ 0 & 0 & 1 \end{bmatrix} \tag{B.4}$$

To reduce the matrix X to the unity matrix, one can start by using the substraction in Eqn. (B.5) on the first and second rows

$$X'_{kj} = X_{kj} - X_{1j}\frac{X_{k1}}{X_{11}} \ , \tag{B.5}$$

and also dividing the first row by X_{11}. These gives the diagonal element of

$$\begin{bmatrix} 1 & \frac{A_{12}}{A_{11}} & \frac{A_{13}}{A_{11}} \\ 0 & A_{22} - A_{12}\frac{A_{21}}{A_{11}} & A_{23} - A_{13}\frac{A_{21}}{A_{11}} \\ 0 & A_{32} - A_{12}\frac{A_{31}}{A_{11}} & A_{33} - A_{13}\frac{A_{31}}{A_{11}} \end{bmatrix} \quad \begin{bmatrix} \frac{1}{A_{11}} & 0 & 0 \\ -\frac{A_{21}}{A_{11}} & 1 & 0 \\ -\frac{A_{31}}{A_{11}} & 0 & 1 \end{bmatrix} \tag{B.6}$$

With further manipulation, the matrix on the left becomes a unity matrix and that on the right becomes an inverse matrix.

Appendix C

Fitting Program - polynomial plus least squares


```
#include "nr.h"
#include <iostream>
#include <fstream>
#include <iomanip>
#include <math.h>
#include <stdlib.h>

#include "gasdev.h"
#include "lfit.h"
#include "gaussj.h"
#include "covsrt.h"
#include "ran1.h"

using namespace std;

// Driver for routine lfit

void funcs(const DP x, Vec_O_DP &afunc)
{
int i;
int ma = afunc.size();
```

```
afunc[0] = 1.0;
afunc[1] = 1.0*x;

for (i=2; i<ma; i++)
{
afunc[i] = afunc[i-1]*x;
}
}

int main(void)
{
//int NPT=100;
const int NPT=14;
int NTERM;
cout << "Enter the number of NTERM:" << endl;
cin >> NTERM;
const DP SPREAD=0.1;
int i,j,k,idum=(-911);
DP chisq;
Vec_BOOL ia(NTERM);
Vec_DP a(NTERM),x(NPT),y(NPT),sig(NPT),yfit(NPT),sigYfit(NPT),sigx(NPT);
Vec_DP xCo56(NPT),yCo56(NPT),sigXCo56(NPT),sigYCo56(NPT);
Vec_DP xCo60(NPT),yCo60(NPT),sigYCo60(NPT);
Mat_DP covar(NTERM,NTERM);

fstream fout, fin, fin1, fout1, fout2, fout3;

//fin.open("edit.dat",ios::in);
fin.open("/home/lutendo/newfit/1496/loglog1496_det2.dat",ios::in);
fout.open("1496_det2.dat", ios::out);
fout1.open("1496_det2_parameters.dat", ios::out);
fout2.open("1496_det2_poly.dat", ios::out);
fout3.open("1496norm_det2.dat", ios::out);
```

```
cout << fixed << setprecision(10);

int kk=0, peaks, peaks1;
if(fin.good())
{
while(!fin.eof())
{
fin >> xCo56[kk] >> yCo56[kk] >> sigYCo56[kk];
if(xCo56[kk] != 0.0)
{
cout << xCo56[kk] << '\t' << yCo56[kk] << '\t' << sigYCo56[kk] << endl;
kk++;
}
}
peaks = kk;
cout << "No of points : " << peaks << endl;
}
else
{
NR::nrerror("Co56 data file not found...");
}


for (i=0;i<NPT;i++)
{
         x[i]=xCo56[i];
y[i] = yCo56[i];
sig[i] = sigYCo56[i];

cout << x[i] << "\t" << y[i] << "\t" << sig[i] << endl;
}

for(i=0; i<NPT; i++)
```

```
funcs(x[i],a);

for(i=0; i<NTERM; i++)
{
// if(i==1)
ia[i] = true;
// else
// ia[i] = false;
}
//cout << "print" << endl;
NR::lfit(x,y,sig,a,ia,covar,chisq,NPT,funcs);

cout << endl << setw(11) << "parameter";
cout << setw(22) << "uncertainty" << endl;
cout << scientific << setprecision(5);

//for  (i=0;i<NPT;i++)
//{
//cout << x[i] << endl;
//}

for (i=0; i<NTERM; i++)
{
cout << " a[" << i << "] = " << setw(8) << a[i];
cout << setw(13)<< sqrt(covar[i][i]) << endl;
}
cout << "chi-squared = " << setw(12) << chisq << endl << endl;
cout << "full covariance matrix" << endl;
// cout << scientific << setprecision(4);

for (i=0; i<NTERM; i++)
{
for (j=0; j<NTERM; j++)
```

```
cout << setw(15) << covar[i][j];
cout << endl;
}

cout << endl << "press RETURN to continue..." << endl;
cin.get();

cout << endl;
// Now check results of restricting fit parameteres
for (i=0; i<NPT; i++)
{
for(j=0; j<NTERM; j++)
yfit[i] += a[j]*pow(x[i],j);
//cout << x[i] << endl;
//sigYfit[i] = a[1]*sig[i];
fout2 << x[i] << "\t" << yfit[i] << endl; // "\t" << sigYCo56[i] << endl;
}

double y_1173=0.0, y_1332=0.0, sig_1173=0.0;
for(j=0; j<NTERM; j++)
{
y_1173 += a[j]*pow(log(1173.228),j);
sig_1173 += ((sqrt(covar[j][j]))*pow(1173.228,j)
  + (a[j])*(j)*(pow(1173,j-1))*(0.003));
y_1332 += a[j]*pow(log(1332.492),j);
}
//cout << exp(y_1173) << "\t" << sig_1173 << endl;

double deltaEsqrd_1173=0.0, deltaEsqrd_1332=0.0;

for(i=0; i<NTERM; i++)
{
// cout << x[i] << endl;
```

```
for(j=0; j<NTERM; j++)
{
deltaEsqrd_1173 += covar[i][j]*pow(log(1173.228),j)*pow(log(1173.228),i);
deltaEsqrd_1332 += covar[i][j]*pow(log(1332.492),j)*pow(log(1332.492),i);
//cout << sqrt(deltaEsqrd) << "\t";
//cout << setw(15) << covar[i][j] << "\t";
}
//cout << endl;
}

double mike, lut;

mike = 1173.228;
lut = 1332.492;

fout3 << mike << "\t" << exp(y_1173) << "\t"
<< exp(y_1173)*sqrt(deltaEsqrd_1173) << endl;
fout3 << lut << "\t" << exp(y_1332) << "\t"
<< exp(y_1332)*sqrt(deltaEsqrd_1332) << endl;


cout << "Now checking results of restricting fit parameters" << endl;
for (i=0; i<NTERM; i+=2)
ia[i]=false;

NR::lfit(x,y,sig,a,ia,covar,chisq,NPT,funcs);
cout << endl << setw(11) << "parameter";
cout << setw(22) << "uncertainty" << endl;
fout1 << endl << setw(11) << "parameter";
fout1 << setw(22) << "uncertainty" << endl;
cout << fixed << setprecision(6);
fout1 << fixed << setprecision(6);
```

```
for (i=0; i<NTERM; i++)
{
cout << " a[" << i << "] = " << setw(8) << a[i];
fout1 << " a[" << i << "] = " << setw(8) << a[i];
cout << setw(13) << sqrt(covar[i][i]) << endl;
fout1 << setw(13) << sqrt(covar[i][i]) << endl;
}

cout << "chi-squared = " << setw(12) << chisq << endl << endl;
cout << "full covariance matrix" << endl;
cout << scientific << setprecision(4);

for (i=0; i<NTERM; i++)
{
for (j=0; j<NTERM; j++)
cout << setw(15) << covar[i][j];
cout << endl;
}
cout << endl;



for(j=0; j<NTERM; j++)
{
y_1173 += a[j]*pow(log(1173.228),j);
sig_1173 += (sqrt(covar[j][j]))*pow(1173.228,j);
y_1332 += a[j]*pow(log(1332.492),j);
// cout << sqrt(covar[j][j]) << endl;
}
// cout << exp(y_1173) << "\t" << sig_1173 << endl;
return 0;
}
}
```

Bibliography

[1] http://home.cern/about/experiments.

[2] R.B. Firestone, L.H. Harwood, R.A. Warner, University of California, Lawrence Berkeley Laboratory Report No. LBL-12219 (unpublished).

[3] C. J. Bowers *et al*, Phys. Rev. **C59**, 1113 (1999).

[4] F. Halzen, A.D. Martin, Quarks and Leptons: An Introductory Course in Modern Particle Physics, John Wiley and Sons, (1984).

[5] W. Greiner, B. Muller, Gauge Theory of Weak Interactions 2nd Ed, Springer-Verlag Berlin Heidelberg, (1996).

[6] D. Griffiths, Introduction to Elementary Particles, John Wiley and Sons, Inc, (1987).

[7] E.D Commins, P.H Bucksbaum, Weak Interactions of Leptons and Quarks, Cambridge University Press, (1983).

[8] G. Kane, Modern Elementary particle Physics, Addison-Wesley, (1993).

[9] T.D. Lee, C.N. Yang, Phys. Rev. **104**, 254 (1956).

[10] C.S. Wu *et al*, Phys. Rev. **105**, 1413 (1957).

[11] M. Goldhaber, L. Grodzins and A.W. Sunyar, Phys .Rev. **109**,1015(1958).

[12] V. Devanathan, Nuclear Physics 2nd Ed., Alpha Science International Ltd., Oxford, U.K., (2006).

[13] D.J. Rowe, J.L. Wood, Fundamentals of Nuclear Models, World Sientic, (2010).

[14] K. Krane, Introductory Nuclear Physics, John Wiley and Sons, (1988).

[15] M.G. Mayer, J.D.H. Jensen, Elementary Theory of Nuclear Shell Structure, John Wiley and Sons, (1955).

[16] C.A. Bertulani, Nuclear Physics in a Nutshell, Princeton University Press, (2007).

[17] S.S.M. Wong, Introductory Nuclear Physics, John Wiley, (1998).

[18] A. Bohr, B.R. Mottelson, Nuclear Structure, vol.1, W.A. Benjamin, inc, (1969).

[19] K.L.G. Heyde, The Nuclear Shell Model 1st Ed, Springer, Berlin Heidelberg, (1990).

[20] R.D. Gill, Gamma Ray Angular Correlations, Academic Press, New York and London, (1975).

[21] B.R. Holstein, Weak Interactions in Nuclei, Princeton University Press, (1989).

[22] R.P. Feynman, M. Gell-Mann, Phys. Rev. **109**, 193 (1958).

[23] M. Gell-Mann, Phys. Rev. **111**, 362, (1958).

[24] B.R. Holstein, Rev. Mod. Phys. **46**, 789, (1976).

[25] S. Weinberg, Phys. Rev. **112**, 1375 (1958).

[26] R. M. Steffen, Phys. Rev. Lett. **3**, 277, (1959).

[27] H. Daniel and G. W. Eakins, Phys. Rev. **117**, 1565, (1960)

[28] B. N. Subba Rao, Nuovo Cimento **20**, 178, (1961)

[29] Z. W. Grabowski, R. S. Raghavan, and R. M. Steffen, Phys. Rev. **139**, B24, (1965)

[30] H. Müller, Nucl. Phys. 74, 449, (1965)

[31] K. S. R. Sastry, R. J. Ouellette, Y. Sharma, and R. Strange, Phys. Lett. **26B**, 207, (1968)

[32] R.B. Firestone, W.C. McHarris, B.R Holstein, Phys. Rev. **C18**, 2719 (1978).

[33] www.nndc.bnl.gov.

[34] C. Iliadis, Nuclear Physics of Stars, Wiley-VCH, (2007).

[35] J.M. Blatt, V.F. Weisskopf, Theoretical Nuclear Physics, Courier Corporation, (1991).

[36] A. Antilla, N. Bisten, E. Arminen, Z. Physik, **234**, 455 (1970).

[37] A.L. Sallaska, PhD Dissertation, University of Washington, (2010).

[38] http://sourceforge.net/projects/jam-daq/.

[39] P.R. Bevington, D.K. Robinson, Data Reduction and Error Analysis for the Physical Sciences, Mc Graw Hill, (2003).

[40] Numerical Recipes in C: The Art Of Scientific Computing, 2nd Ed, Cambridge University Press, (1992).

[41] A.L. Sallaska *et al*, Phys. Rev. **C83**, 034611, (2011).

[42] F. Salvat, J.M. Fernandez-Varea, J. Sempau, PENELOPE-2008: A code system for Monte Carlo Simulation of Electron and Photon Transport (OECD Publications, Paris, 2008).

[43] J.W. Martin, J. Yuan, S.A. Hoedl, B.W. Filippone, D. Fong, T.M. Ito, E. Lin, B. Tipton, and A.R. Young, Phys. Rev. **C73**, 01550, (2006).

[44] M. Bhattacharya *et al*, Phys. Rev. **C77**, 065503, (2008).

[45] E.K. Warburton, A.R. Poletti, J.W. Olness, Phys. Rev. **168**, 1232, (1968).

[46] A. Kontos *et al.*, Phys. Rev. C**86**, 055801, (2012).

[47] J. C. Hardy and I. S. Towner, Phys. Rev. C**91**, 025501 (2015).

[48] K. Minamisono *et al.*, Phys. Rev. C**84**, 055501 (2011).

[49] W. Richter, private communication.

[50] D. MacArthur, A. J. Brown, P. A. Butler, L. L. Green, C. J. Lister, A. N. James, P. J. Nolan, and J. F. Sharpey- Schafer, Can. J. Phys. **54**, 1134 (1976).